A novel manufacturing process and validated predictive model for high-strength and low-residual stresses in extra-large 7xxx panels

Jing-Hua Zheng [a,*], Ran Pan [b], Robert C. Wimpory [c], Jianguo Lin [a], Chen Li [d], Catrin M. Davies [a]

[a] Department of Mechanical Engineering, Imperial College London, London SW7 2AZ, UK
[b] AVIC Manufacturing Technology Institute, Beijing, PR China
[c] Helmholtz-Zentrum Berlin für Materialien und Energie, Hahn-Meitner-Platz 1, 14109 Berlin, Germany
[d] The First Aircraft Institute, Xi'an, PR China

HIGHLIGHTS

- A novel manufacturing process was developed to mitigate part distortion in T-section panels.
- Low and controllable residual stresses within ~ 100 MPa were successfully achieved by the process.
- Integrated FE model, covering the entire process, was established and validated by the experimental data.
- Both residual stresses and the final yield strength distributions were accurately predicted.
- The suggested processing parameters are 1.5% cold rolling and 13 h constrained ageing.

GRAPHICAL ABSTRACT
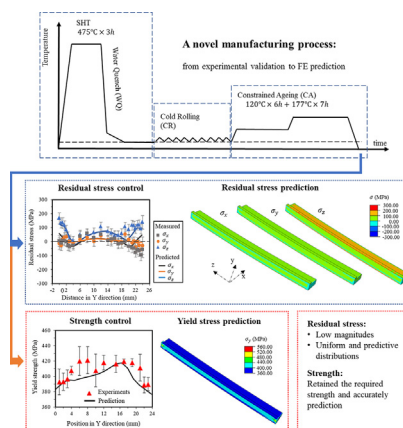
ARTICLE INFO

ABSTRACT

A novel manufacturing process, enabling the production of high quality (i.e. with low and controllable residual stress (RS) distributions and good mechanical properties) T-section 7xxx panels, has been established. This process provides a solution to residual stress induced distortion problems, which greatly concerns a range of industries, especially the aircraft industry. This process consists of three sequential steps — water quenching (WQ), cold rolling (CR) and constrained ageing (CA). The effectiveness of this process was experimentally verified through applying this process to laboratory sized 7050 T-section panels. The RS was measured by neutron diffraction and X-ray techniques, in addition to deflections and hardness at each processing stage. An integrated Finite Element (FE) model, including all three steps, was developed to simulate this manufacturing process and predict both the RS and the final strength distributions. It has been concluded that this novel process can effectively reduce the residual stresses from ± 300 MPa to within ± 100 MPa and produce T-section panels with required mechanical properties (i.e. hardness: ~159 HV_{10}). A cold rolling level of 1.5% was found most appropriate. The residual stress and yield strength distributions were accurately predicted by FE, providing a valuable prediction tool to process optimization for industrial applications.

* Corresponding author.
E-mail address: jinghua.zheng13@imperial.ac.uk (J.-H. Zheng).

1. Introduction

Al-Zn-Mg-Cu alloys, such as 7050, are widely used as structural materials in the aviation industry, due to their excellent mechanical properties, especially their high strength-to-weight ratio [1]. The mechanical properties of these 7xxx series alloys rely on an appropriate heat treatment process, which includes solution heat treatment, quenching and ageing, such that the optimal properties can be achieved [2]. Thus, to produce an aircraft part with both the required dimensions and the optimal mechanical properties, the conventional manufacturing process usually incorporates a heat treatment process in between the initial forming (e.g. hot forging, hot rolling, etc.) and the final machine finishing [3]. However, one of the greatest problems induced by the heat treatment process is the large residual stresses generated by quenching [4–7]. Quenching is necessary to lock the heat treatable aluminium alloy into a super saturate solid solution state and in preparation for the subsequent age hardening. Unfortunately, the rapid cooling process (i.e. quenching) also induces a severe thermal gradient through the part's thickness, leading to a large residual stress field, which is detrimental to the final structural integrity and dimensional accuracy [8,9]. The residual stresses are raised from the non-homogeneous plastic flow of the material, where the interior material cools slower than the surface one and tries to thermally contract, however, is constrained by the cooler surface material, leaving large tensile stresses in the core and compressive stress near the surface [5,8]. Residual stresses and subsequent distortion have been a major industrial issues for decades, especially when producing extra-long and thick aircraft panels, such as aircraft wing joints, with uniform cross sections, leading to substantial costs in re-work or scrappage. Hence an advanced manufacturing route to produce these parts with low residual stresses as well as optimal mechanical properties is essential.

Methods, that are solely used to reduce the residual stresses, have been well established. Cold working, where a uniform plastic deformation is applied to the quenched part, is an efficient method used for industrial-sized (i.e. extra-large) aluminium components. Altschuler et al. [10] have quantitatively investigated the residual stress reduction from cold working and has demonstrated its efficiency in significant residual stress reduction. Robinson et al. extensively studied the cold compression effects on the residual stress reduction in 7075 [4], and 7449 [11], and found that compression ratios of 1%–4% are beneficial in reducing the residual stress magnitude from a range of ~ −300 to +300 MPa, created by quenching, to a range of ~ −100 to 20 MPa. Other RS relief techniques, such as the thermally induced stress relaxation, have also been widely investigated by several researchers, such as Orner and Kulin [12] and Robinson et al. [13] etc. However, elevated temperature stress relief is not suitable for heat treatable aluminium alloys, as it may lead to a notable sacrifice on the material's strength. As reported by Kulin [12], elevated temperatures can enhance stress relaxation, but significantly reduce the material strength due to the severe over-ageing. Additionally, research has also been performed to study the effects of machining [14] and optimize its parameters in turning [15] and cutting [16,17]. Such research has provided some valuable conclusions regarding the effectiveness of their studied techniques (e.g. cold compression [4,18], retrogressive and re-ageing (RRA) [19], uphill quenching [20,21], increasing quenchant temperature [22], post quenching delay [23], etc.) to reduce the residual stress. However, for industrial manufacturing processes, the situations are much more complex. Generally, the manufacturing process is expected to include various steps, such as forming, heat treatments, residual stress reduction, etc. in an appropriate order, to produce the parts and guarantee their final properties as well as accurate dimensions. The selection of each step and their sequence in the manufacturing process should be appropriately arranged to maximise their effectiveness, facilitate their uptake by industry, while minimising any detrimental effects of the former treatments on the subsequent processing stages. Though previous research has individually studied some steps in isolation, they have not

provided a reliable and practical route that can be implemented directly in current industrial manufacturing processes. Therefore, it is essential to establish a novel and advanced manufacturing process that can produce qualified parts which address the issues caused by residual stress.

The conventional manufacturing process to produce extra-large aluminium components involves: Hot forming (e.g. hot forging) → Solution Heat Treatment (SHT) → Quenching → cold compression (e.g. cold forging) → T74 ageing → machine finishing. This process has demonstrated its efficiency to produce some low-residual stress, extra-large parts with simplified dimensions (such as rectangular structures [4]), that can easily be cold compressed to relieve most quenching induced residual stresses. However, for those extra-long aircraft panels, which are widely used as wing connections, such as T wing-joints [24] (i.e. up to 5 m long while ~120mm thick), the process is no longer applicable. This is attributed to the extra-long geometry, where no such cumbersome mould can cover the whole area of the panels to produce a uniform plastic deformation at the cold compression stage. Instead, most industries apply a multi-step cold compression technique, such as multi-step cold forging, which use a small-sized mould to sequentially compress different regions of a part until the optimal average plastic deformation is acheived. These multiple compressions, again, raise undesirable residual stresses in the over-lap regions, where the material has been compressed more than once. As reported by Pan, et al. [25], the overlaps significantly raise the residual stresses in that region, and therefore it is difficult to predict and control the residual stress distribution by the multi-compression method causing increased scrappage rates. In addition, the standard ageing techniques applied have not fully realised the residual stress reduction potential.

In this work, a novel process is established, newly enabling long, thick aircraft structures to be manufactured with the required mechanical properties and concurrently low and controllable residual stresses. The novel process involves solution heat treatment, water quenching, cold rolling and a subsequent constrained ageing treatment. The effectiveness of the proposed manufacturing process to produce high quality panels is verified by applying this process to laboratory sized 7050 T-sectional panels that represent a scaled down version of the aircraft wing panel T-joint, which is a typical component that experiences issues with residual stresses and distortion. The residual stresses, surface height profile, and hardness values at each processing stage have been measured using the neutron & X-ray diffraction technique, digital height gauge and Vickers hardness tester, respectively, to examine the RS evolution, dimensional stability and mechanical properties in the process. The mechanisms and experimental phenomenon of the residual stress distributions and the hardness distributions have been discussed in detail. In addition, integrated finite element (FE) models have been developed, including a quenching, cold rolling and constrained ageing model, of the T-panel to predict the RS distribution at each processing stages and to predict the final yield strength distribution after ageing. These models have been validated through comparison with the experimental measurements and provide a valuable industrial tool to design and optimize the processing routes for a range of component geometries.

2. Experiments

2.1. Material, sample geometries and procedures of the manufacturing process

Aluminium alloy 7050 was used in this study, of chemical composition 5.7–6.7 wt% Zn, 1.9–2.6 wt% Mg and 2–2.6 wt% Cu. This material was supplied by the First Aircraft Institute (FAI) that represents that used in industrial-sized T-joint components (i.e. 120mm in thickness and ~5 m in length), which are used to connect the aircraft wing panels. Several scaled-down T-section panels were milled from the material provided, the dimensions of which are illustrated in Fig. 2(a). These T-panels consist of one web and two flange parts of thickness 24 mm

and 16 mm, respectively. The T-panels were 450 mm in length to ensure that a steady state region was achieved, where the resultant material properties are approximately uniform along its length, after each stage of the manufacturing process.

The temperature profile of the manufacturing process, together with the corresponding images of each step (i.e. water quenching, cold rolling and constrained ageing), are illustrated in Fig. 1(a). The principles and mechanisms of the three stages in this new process, including the detailed processing procedures are described below:

(i) Solution heat treatment and water quenching (WQ)

T-section panels were solution heat treated (SHT) at 475 °C for 3 h, and then quenched in cold water at ~20 °C. The quenching direction is in the transverse (X co-ordinate) direction, as shown in Fig. 2(a). In the aircraft industry, warm water ~60–70 °C is usually used as the quenchant for aluminium alloys to minimise the generation of RS [19]. However, here, due to small size of scaled down T-section panel, cold water (~20 °C) was adopted to enable sufficient quenching-induced RS and facilitate the subsequent examination of RS reduction. All quenched T-section panels were then kept at room temperature for 7 days until the microstructures were considered stable and relatively unaffected by subsequent natural ageing during cold rolling. Two of the T-panels were then stored for future measurements, while the others were progressed to the next manufacturing step. For clarity, "WQ" is adopted to represent the condition, where both water quenching and 7 days room temperature delay were applied to the part.

(ii) Cold rolling (CR)

The selected WQ T-section panels were then cold rolled to generate an average deformation level of 1.5% and 3%, using the set of rollers presented in Fig. 1(b). Both rollers had a nominal diameter of 78 mm and rotated at an angular velocity of 1 rads^{-1}. The bottom roller contained a groove to accommodate the webbed region of the T-section panel. The aim of CR is to apply relatively uniform plastic deformation through the thickness of the panels for RS reduction. More importantly, the deformation employed is continuous and uniformly distributed along the panels' length, thus, expecting to achieve controllable and homogenous residual stress distributions. The notation "WQ + CR" is adopted to represent the condition, where quenching, a room temperature delay and cold rolling were applied. After CR, two of the T-section panels under each condition: WQ + CR (1.5%) and WQ + CR (3.0%) were stored, while the others were prepared for the next constrained ageing treatment.

(iii) Constrained ageing (CA)

Subsequently, the WQ + CR T-section panels, both with 1.5% and 3.0% CR levels, were constrained at a fixed displacement using the clamping tool shown in Fig. 1(c). To maintain the curvature created by the prior cold rolling step (i.e. 1.5%, 3.0%), the bottom supports were adjusted before CA. Thermo-couples were distributed along the longitudinal direction of the T-panel to monitor the temperature variation during CA. The clamped T-panels were then placed in the middle of the oven and aged at 120°C × 6h + 177°C × 7h to achieve the target T74 mechanical properties (i.e. acceptable strength and enhanced corrosion resistance), as well as further minimise the RS. The ageing condition adopted here is according to the T74 ageing standard [26]. This treatment is expected to maximise the RS reduction, correct the panels' shape and improve the mechanical properties of the material. This new ageing method was inspired by the creep age forming process [27–29], where creep strain continuously increases at the ageing temperature, while precipitation occurs concurrently. Interactions between the dislocations, created by cold rolling and stress relaxation, and the precipitation process also occur.

After employing the above manufacturing process, the T-section panels under each processing conditions: WQ, WQ + CR (1.5%), WQ + CR (3.0%), WQ + CR (1.5%) + CA, WQ + CR (3.0%) + CA T-panels were achieved. These T-section panels were then prepared for the RS and surface profile measurements.
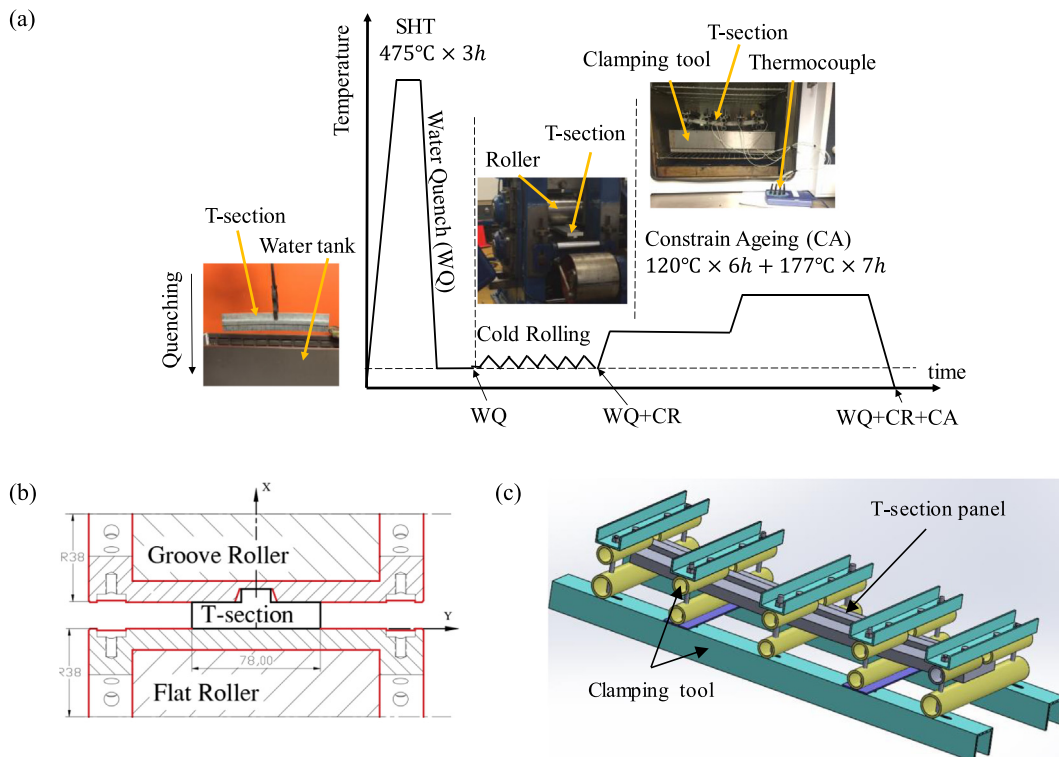

Fig. 1. Schematic illustration of the (a) manufacturing process, (b) rollers and (c) constrained ageing clamping tool.
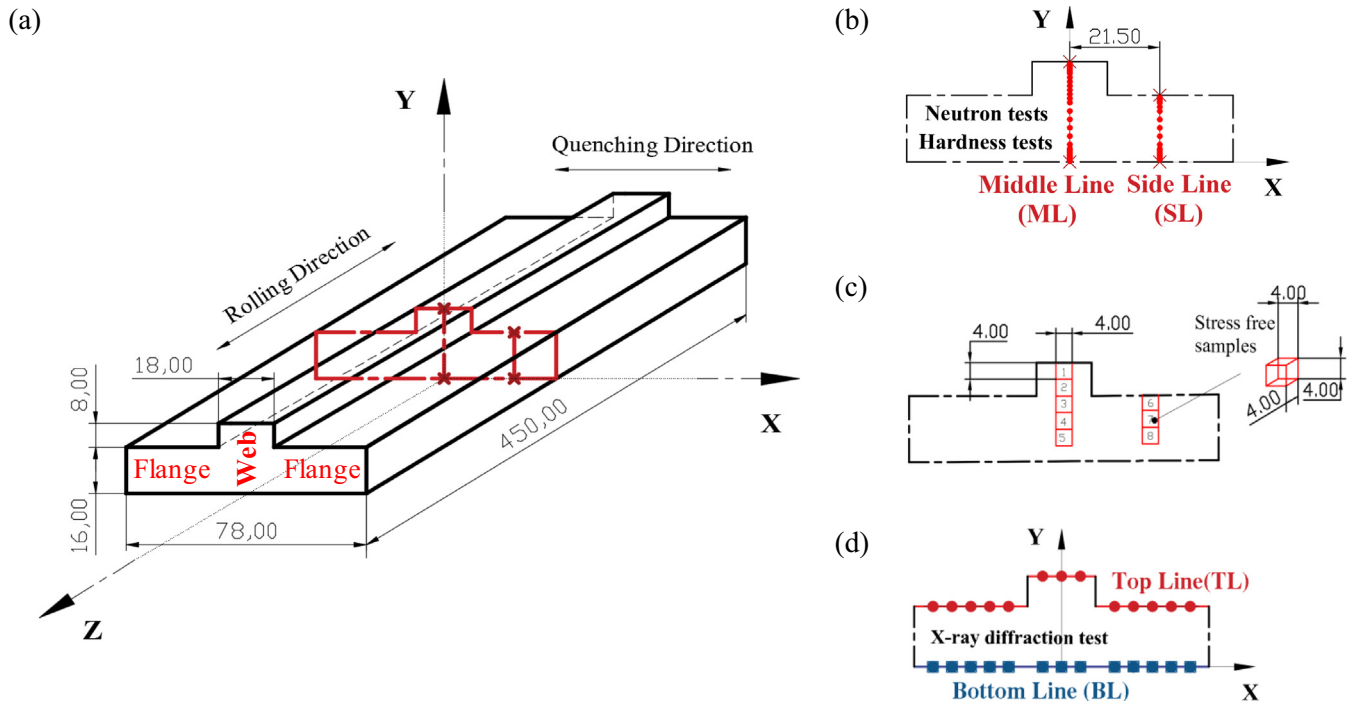
(a)

(b)

(c)

(d)

Fig. 2. (a) Dimensions (in mm) and measurement plane of the lab-sized T-panels, (b) neutron diffraction measurement points, (c) locations and dimensions of the stress-free samples (d) X-ray diffraction measurement points.

2.2. Residual stress characterization (Neutron and X-ray tests)

Neutron diffraction (ND) measurements were performed on three T-section panels: (i) water quenched (WQ), (ii) water quenched and 1.5% cold rolled (WQ + CR (1.5%)), (iii) water quenched, 1.5% cold rolled and constrained aged (WQ + CR (1.5%) + CA). Measurements were performed on the neutron strain scanner instrument E3 at the Helmholtz-Zentrum Berlin. Measurements were performed at 26 and 19 points along the middle line (ML) and side line (SL), respectively, as shown in Fig. 2(a–b), to examine the through depth RS distribution in both the web and the flange parts. Measurements were taken at 0.5 mm intervals near the surfaces, while increasing increment size to 2 mm at the core. The small increments near the surface are necessary to capture the large RS gradient created by the rolling process. In addition, the measurement points located within 2 mm from the surface were measured twice at 0° and 180° relative to the bisecting angle between incident and diffracted beams and averaged to minimise pseudo-strain errors.

A gauge volume, $2 \times 2 \times 2 mm^3$, was used to sample sufficient grains for a satisfactory statistical average diffraction peak to be measured, while obtaining adequate resolution of the RS distribution. The neutron wave length was $\lambda = 1.47$ Å. The scattering angle, 2θ, was obtained from the {311} peak ($2\theta \approx 74°$) for calculating the lattice spacing, d, using Bragg's Law [30,31] in Eq. (1). The scattering angle, $2\theta_0$, of the strain-free samples were obtained by measuring small cubes ($4 \times 4 \times 4$ mm^3), which were cut from three nominally identical T-section panels as those measured in the corresponding locations, shown in Fig. 2(c). These values (i.e. $2\theta_0$) are used to calculate the strain free lattice spacing, d_0, using Eq. (1), and subsequently used as the reference lattice spacings for the calculation of the elastic residual strains, using Eq. (2).

$$m\lambda = 2d_{hkl} \, sin\theta_{hkl} \tag{1}$$

$$\varepsilon_{hkl} = \frac{\Delta d_{hkl}}{d_{0,hkl}} = \frac{sin\theta_{0,hkl}}{sin\theta_{hkl}} - 1 \tag{2}$$

where d_{hkl} and $d_{0,\,hkl}$ are crystallographic plane specific lattice spacings of the samples measured and strain free samples, respectively, θ_{hkl} and $\theta_{0,\,hkl}$ are the corresponding scattering vectors, λ is the wave length and m is an integer. Substituting Eq. (1) into Eq. (2), the lattice spacing values can be eliminated and the elastic residual strains can be directly calculated using the measured scattering angles without a calculation of the lattice spacings. The residual stresses in x, y, z directions then can be determined from the corresponding measured residual strains using Hookes law, Eq. (3).

$$\sigma_{ii} = \frac{E_{hkl}}{(1 + v_{hkl})(1-2v_{hkl})} \left[(1 + v_{hkl})\varepsilon_{ii}^{hkl} + v_{hkl} \left(\varepsilon_{jj}^{hkl} + \varepsilon_{kk}^{hkl} \right) \right] \tag{3}$$

where E_{hkl} and v_{hkl} is the elastic modulus and Poisson's ratio, respectively, of a specific crystallographic plane. The elastic modulus, 69.0 GPa, and Poisson's ratio, 0.33, for aluminium alloy [26] was taken for calculations in all directions.

X-ray diffraction measurements were performed on five T-section panels: (i) WQ, (ii) WQ + CR (1.5%), (iii) WQ + CR (3.0%), (iv) WQ + CR (1.5%) + CA, (v) WQ + CR (3.0%) + CA, via the Pulstec μ-X360 [11,32], to assess the near surface residual stresses in the rolling (z co-ordinate) direction during the process. Additionally, the effects of cold rolling levels on RS reductions were examined by comparing the RS between state (ii) and (iii). This technique calculates the residual stresses using Bragg's Law, however, can only detect the in-plane RS in the surface layer, where plane stress assumption is applicable. The measurements were taken at 5 mm intervals along the top line (TL) and bottom line (BL) in the mid plane, shown in Fig. 2(d).

2.3. Surface profile and hardness testing

The surface profile of CR and CR + CA T-section panels at Z = 0, ±20, ±60, ±140, ±225 mm, were measured using a digital height gauge to examine the parts' dimensional stability after CR and CA. For each Z-axis position, 3 measurement points at 10 mm intervals (in Y-axis) were averaged to improve measurement accuracy. Finally, the mid planes of the T-panels at WQ, WQ + CR (1.5%) and WQ + CR (1.5%)

+ CA stages were sectioned out and Vickers hardness tests were performed on these sectioned mid planes at the positions illustrated in Fig. 3. On a given line through the thickness, hardness measurements were taken at 2 mm intervals at the core and at an increment of 1 mm near the surface, where higher gradients in properties are expected. At each Y measurement location, 3 indentations, which were 1.5 mm apart from each other in X-direction, were averaged. The hardness tests were performed at room temperature using Indentec Model 8187.5 LKV Universal Hardness Tester, with a weight of 10 kg.

A measurement matrix, including all measurement tests on T-sectional panels at different processing stages, is given in Table 1. X-ray diffraction tests were performed on all T-sectional panels under WQ, WQ + CR and WQ + CR + CA conditions, including two CR levels (i.e. 1.5% and 3.0%), to verify the effectiveness of the process and examine the effects of CR levels on RS reduction. Due to the limited access time to the neutron strain scanner instrument, the neutron diffraction tests were only performed on T-sectional panels under WQ, WQ + CR and WQ + CR + CA, conditions with a CR level of 1.5%, since 1.5% has been found most effective for RS reduction [33]. Hardness measurements were performed on the same T-section panels that neutron diffraction measurements were performed on to examine the evolution of mechanical properties. Deflection measurements were conducted on all test conditions to check the surface profiles.

3. Experimental results

3.1. Surface residual stresses at each stage by the X-ray diffraction technique (cold rolling = 1.5% and 3.0%)

Fig. 4 presents the surface RS profiles in the rolling direction, σ_z, along the top line (TL) and bottom line (BL) of the T-section panels (see measurement locations in Fig. 4(e)) at each processing stage, where the average thickness reduction produced by CR is (a, b) 1.5% and (c, d) 3.0%. The blue circular symbols represent the surface residual stress values directly after the water quenching (WQ). The orange square symbols represent the surface residual stress values after both WQ and the cold rolling (CR). The green triangles represents the surface residual stresses after WQ, CR and the constrained ageing (CA) As shown in Fig. 4(a), relatively uniform RS distributions were observed for the T-panels at all processing stages. No significant differences were observed between the RS values on the web surface (i.e. X = −5 to 5 mm) and that on the flange surface (X < −5 and >5 mm). Compressive RS, which fluctuates around −200 MPa, were created on the parts' surface (i.e. TL and BL) by WQ. This value agrees well with several researchers that have studied quenching induced RS on 7xxx alloys, such as [4,19,34]. The compressive surface RS were created due to the thermal gradient during cooling (i.e. quenching), which results in a non-uniform plastic flow of the material, leaving high tensile stresses in the core while compressive stresses at the surfaces [7]. The RS becomes tensile with a magnitude of around 200 MPa after 1.5% CR. The increase is attributed to the significant surface shear during rolling. Though an average thickness reduction of 1.5% was achieved after CR,
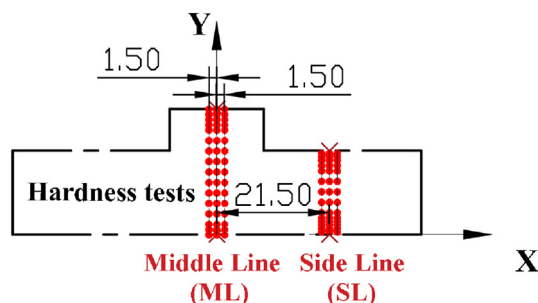

Fig. 3. Schematic illustration of the hardness measurement locations.

a plastic strain gradient through the panel's thickness exists, where relatively uniform compressive strains (in the thickness direction) are present in the core, while large tensile strains (in the rolling direction) are present near the surface. Therefore, the panel's surfaces are severely stretched in the rolling direction by the friction force, leaving high tensile surface RS up to ~200 MPa. In addition, more dislocations were introduced to the surface region of the panel by CR, thus are expected to facilitate the surface stress relaxation in the subsequent CA process, according to [35]. Therefore, larger RS reduction is expected in the surface region during CA. As can be seen in Fig. 4(a), after CA, the RS finally reduces to around ~100 MPa due to the thermally activated stress relaxation phenomena at the ageing temperature (i.e. 120°C × 6h + 177°C × 7h).

Comparing the σ_z values of the T-panels along the BL in Fig. 4 (b) with that along the TL in Fig. 4(a), it can be observed that similar WQ induced surface RS values were measured (i.e. −200 MPa). However, for the T-panels in the WQ + 1.5%CR stage, the average RS values (~230 MPa) on the bottom surface (i.e. BL) are slightly larger than that (~200 MPa) on the top surface (i.e. TL). Though there is some uncertainty associated with the measurements, these trends were confirmed by the T-panel measurements after WQ + 3.0%CR. In addition, neutron diffraction results also showed the same phenomenon, where larger RS values were present on the bottom surface, which will be later described. This phenomenon can be attributed to the distinct top and bottom surface shear stress levels. Though the angular velocities of the two rollers are identical, different line velocities were employed during rolling due to smaller radius of the roller in the groove region. The top surface of the web was sheared less than the bottom surface. In addition, the lower shear stress levels on the top web surface constrains the deformation of the top flange surface, leading to curved T-panels after the cold rolling. The detailed curvature profile is later presented in Fig. 12. Therefore, lower shear stress levels were achieved not only on web of the TL, but also on the flange of the TL, leading to smaller σ_z at the TL comparing to that of the BL. The "web" and "flange" of the T-section are illustrated in Fig. 2(a). Comparing the RS distributions along BL and TL for the T-panels at the WQ + 1.5CR + CA stage, it can be concluded that similar final RS values, which are around 100 MPa, are generated. It should be noted that, though the surface RS modified by 1.5%CR are higher on the BL than that on the TL, they were all reduced to around ~100 MPa after the final constrained ageing treatments, indicating larger reductions in RS magnitudes on the bottom surface. The experimental results from the Stress Relaxation Ageing (SRA) tests [35] showed that larger pre-strain values can create more mobile dislocations that facilitate the stress relaxation process, leading to larger stress reduction after the ageing treatment. Here, the plastic deformations in the bottom region created by cold rolling are larger than that in the top surface region. Therefore, the larger stress reduction on the bottom surface during CA may be attributed to the larger prior plastic strains on BL compared to that on the TL.

Fig. 4(c) and (d) illustrate the surface RS distribution, σ_z, along the top and bottom lines of the T-panel, respectively, where the cold rolling level applied was 3.0%. The surface RS changed from around −200 MPa to around 200–300 MPa after cold rolling, then reduced to around 100–150 MPa after constrained ageing. Similar to the case of 1.5%CR, the RS values at WQ + 3.0%CR + CA stage are nearly identical (i.e. around 100–150 MPa) along TL and BL of the T-panels. However, comparing the RS values at the WQ + 3.0%CR stage along BL and TL, higher RS values were observed along BL (in Fig. 4(d)) than that along TL (in Fig. 4(c)). The average RS value along BL is ~300 MPa after 3.0% CR, while ~200 MPa along TL. The cause of the phenomenon is also due to the different plastic strain levels created by CR on the BL and TL. After CA, the RS along TL and BL are all reduced to around 100–150 MPa.

Comparing the σ_z evolutions during the above two manufacturing process (i.e. WQ + 1.5%CR + CA, WQ + 3.0%CR + CA), it can be observed that higher RS distributions were created by higher cold rolling levels, due to the larger shear stresses on the panel's surface. The σ_z

Table 1
Measurement details on the T-section panels.

Processing stages	Residual stress measurement		Hardness measurement	Deflection measurement
	X-ray diffraction	Neutron diffraction		
WQ	✓	✓	✓	✓
WQ + CR (1.5%)	✓	✓	✓	✓
WQ + CR (1.5%) + CA	✓	✓	✓	✓
WQ + CR (3.0%)	✓			✓
WQ + CR (3.0%) + CA	✓			✓

values of WQ + 3.0% CR are 200–300 MPa after the component being subjected to WQ + 3.0%CR, while are ~200 MPa after WQ + 1.5%CR. Given the fixed CA time and temperature, the high RS values created by 3.0% CR cannot be sufficiently reduced by CA, leaving final RS values of 100–150 MPa, which are larger than that (i.e. within ~100 MPa) in the WQ + 1.5% + CA panel. Therefore, it can be concluded that 1.5% CR is most appropriate to achieve uniform compressive strains at the panel's core. After CR, a slight decrease in the RS values, with an increase in X, is somewhat apparent in Fig. 4, though the measurements are expected to be symmetric about the Y axis. This may be attributed to the slight
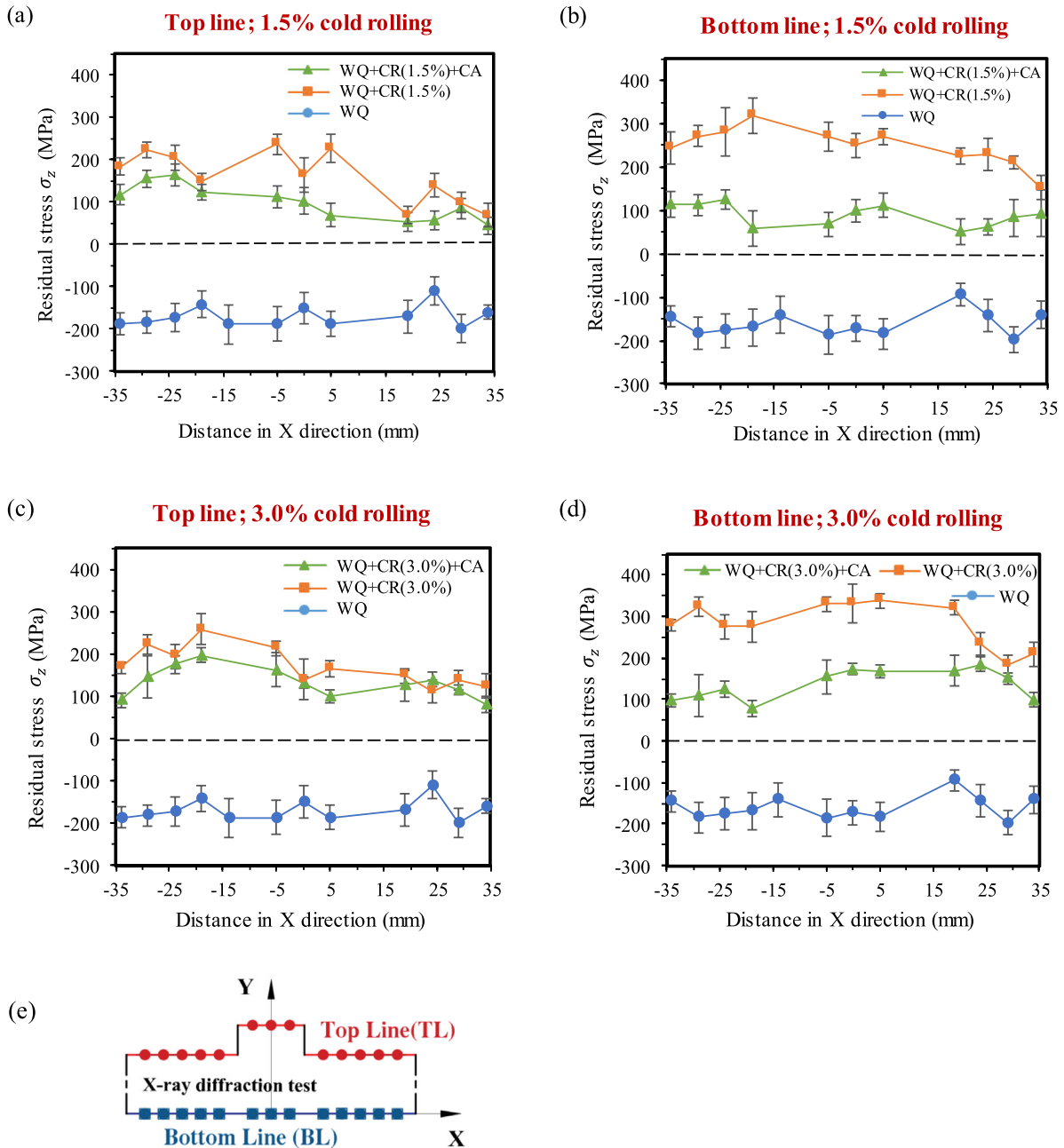

Fig. 4. Residual stresses in the rolling direction (i.e. σ_z) along the (a) top line and (b) bottom line of the T-section panels at water-quenched (WQ), cold-rolled (WQ + CR) and constrain-aged (WQ + CR + CA) stages: The cold rolling level is (a), (b) 1.5% and (c), (d) 3.0%; (e) A schematic illustration of the top line (TL) and bottom line (BL).

misalignment between the T-section panel and the roller during the cold rolling process, leading to a slight difference in the thickness reduction ratio on both sides of the flange (i.e. Fig. 2). This minor trend is not the focus of the work, where obvious differences were still observed when comparing the residual stresses after WQ, CR and CA, and are good illustrations of the effectiveness of the process. Additionally, the effects of cold rolling levels can be seen, where high RS distributions were observed in T-section panels with higher cold rolling levels.

3.2. Through depth residual stresses at each processing stage via neutron diffraction technique (cold rolling = 1.5%)

3.2.1. d_0 determination

Fig. 5 illustrates the strain free scattering angles, $2\theta_0$, in 3 orthogonal (x, y, z) directions, along the middle line (ML) and the side line (SL) of the T-panels at WQ, WQ + CR and WQ + CR + CA stages, here denoted $\theta_{0, wq}$, $\theta_{0, cr}$, $\theta_{0, ca}$, respectively. The black, blue and red columns present the $2\theta_0$ values of the T-panels at WQ, WQ + CR and WQ + CR + CA stages, respectively. Solid, cross-hatched, and hatched markings represent the $2\theta_0$ in x, y and z direction, respectively. These are presented to identify any trends with position, orientation and processing route. These strain-free lattice spacings are used to calculate the residual stresses using Eqs. (1)–(3), as described in Section 2.2. Generally, larger scattering angles (i.e. $2\theta_{0, ca} = $ ~74.09°) were determined for the WQ + CR + CA T-panel compared to that for the strain-free WQ (i.e. $2\theta_{0, wq} = $ ~74.02°) and WQ + CR (i.e. $2\theta_{0, cr} = $ ~74.02°). Considering the $2\theta_0$ values through the thickness (both along ML and SL) under identical processing conditions, no apparent trends were observed, where all values fluctuated around a mean value. Similarly, no obvious differences and trends were observed for $2\theta_0$ values in x, y, z directions. Therefore, the average value of $2\theta_0$ was used for the subsequent RS calculation [19].

The average $2\theta_0$ and the corresponding lattice spacing values are given in Table 2.

In terms of WQ T-panels, the average strain free lattice spacings, $d_{0, wq}$, was calculated by substituting $\lambda = 1.47$Å and average value of $2\theta_{0, wq}$ into Eq. (1), and hence $d_{0, wq} = 1.2211 \pm 0.0002$Å. This $d_{0, wq}$ value is expected to be slight smaller than that, d_{Al}, of the pure Al matrix due to the internal stress field created by the interphase boundaries between GP zones and Al-matrix [26]. After quenching, Zn, Mg, etc. elements were dissolved and locked into the Al-matrix. Fully coherent GP zones were formed during the room temperature delay. These GP zones create lattice strain field and hence micro-stresses across the interphase boundaries, which may lead to a decrease in the lattice spacing. However, in this case, no obvious differences were found between the calculated $d_{0, wq}$ (i.e. $d_{0, wq} = 1.2211 \pm 0.0002$Å) and d_{Al} (i.e. $d_{Al} = 1.2211$Å) [36]. This may because the effects of the GP zones, created by the room temperature delay and are extremely small. This GP zone induced strain field may be mixed with the systematic error of the ND instrument, and thus, no difference was observed.

For WQ + CR T-panels, though no significant variations were observed in $2\theta_{0, cr}$ along ML and SL, the material was significantly deformed by cold rolling, especially near the surface. This plastic strain history introduces dislocations into the structure which can lead to peak broadening which leads to higher uncertainties in the Gaussian fit to the intensity peak. The magnitude of the out-of-plane stresses, σ_y, at the surface were found to be significantly larger than zero when using the average value of $2\theta_{0, cr}$, in the residual stress calculations, which was deemed unreasonable. Therefore, $2\theta_{0, cr}$ was taken to be 74.034°, which is within the uncertainty range of $2\theta_{0, cr}$ (i.e. 74.016 ± 0.020°), to ensure the surface out of plane RS value, σ_y, ≈0MPa.

As observed above, larger $2\theta_{0, ca}$ values were measured for WQ + CR + CA T-panels, which indicates a smaller average lattice spacing for the
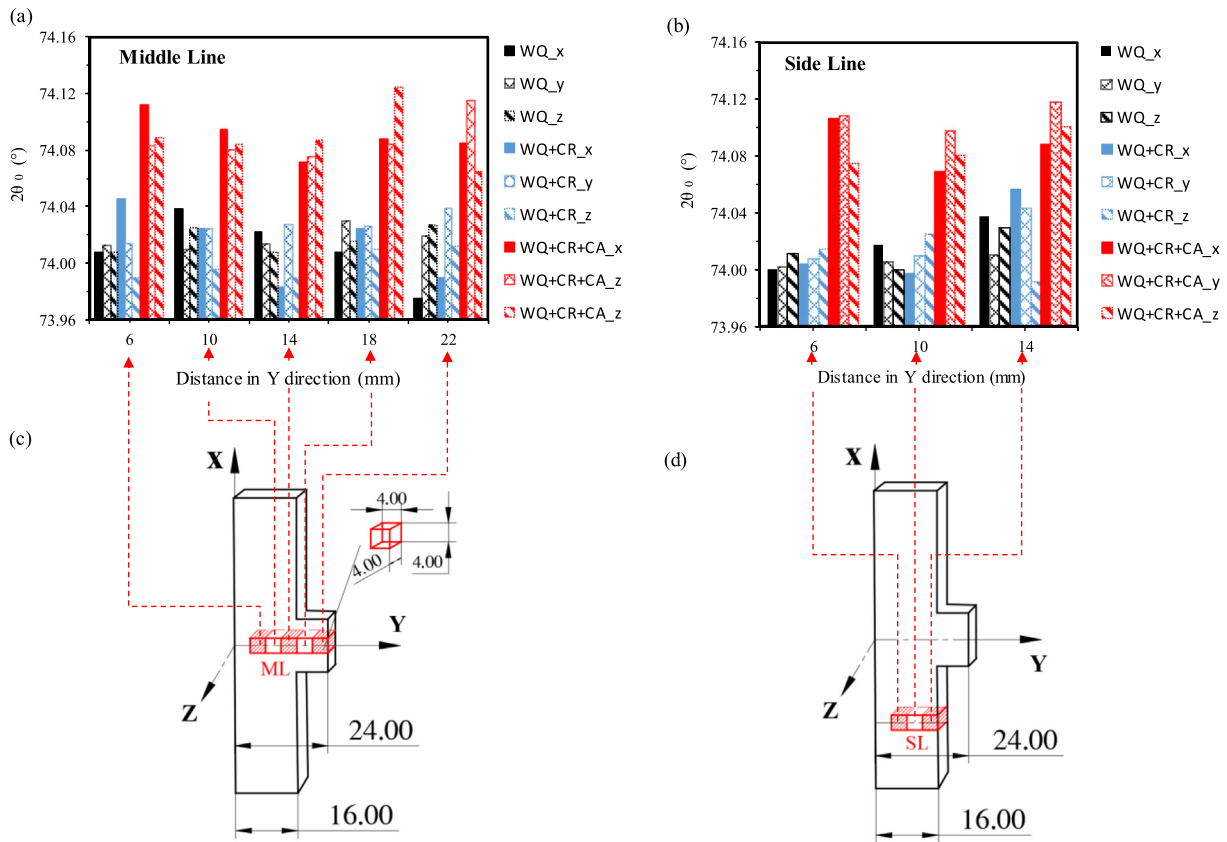

Fig. 5. $2\theta_0$ values along (a) the middle line and (b) the side line. The corresponding locations of the stress-free samples along (c) the middle line and the (d) side line. Note that WQ, CR and CA stands for treatments: water-quenching (WQ), cold-rolling (WQ + CR) and constrain-ageing (WQ + CR + CA), respectively. x, y, z represent the 3 orthogonal directions. The cold rolling level was 1.5%.

Table 2
$2\theta_0$ and d_0 used for RS calculation at WQ, WQ + CR, WQ + CR + CA stage.

	WQ	WQ + CR	WQ + CR + CA
$2\theta_0(°)$	$2\theta_{0, wq}$	$2\theta_{0, cr}$	$2\theta_{0, ca}$
	74.014 ± 0.014	74.016 ± 0.020	74.090 ± 0.016
$d_0(Å)$	$d_{0, wq}$	$d_{0, cr}$	$d_{0, ca}$
	1.2211 ± 0.0002	1.2208 ± 0.0003	1.2200 ± 0.0002

{311} planes after the constrained ageing treatment. This smaller lattice spacing, $d_{0, ca}$, should be attributed to the formation of the incoherent precipitates, η, at the ageing temperatures, making the lattice spacing of Al smaller.

3.2.2. Residual stress distributions

The RS distributions along the middle line for WQ, WQ + CR and WQ + CR + CA conditions are presented in Fig. 6, where the squares, circles and triangles represent the RS in X, Y and Z directions, respectively. In general, the RS generated by quenching, which ranged from −250 MPa to +250 MPa, became from −100 to +270 MPa by cold rolling, and was generally further reduced to a range of −95 to +165 MPa by constrained ageing. As generally accepted, the quenching induced RS are attributed to the large thermal gradient from the centre to the surface of the material during cooling, leading to a sequential thermal contraction from the surface to the central part and hence a non-uniform plastic flow of the material. During the initial stage of quenching, the surface material cools much faster than the interior. Plastic deformation can be achieved near the surface due to thermally induced stresses, leaving a region of large tensile residual stresses at the surface balanced by relatively small compressive residual stresses in the core. At this point, the component consists of a soft hot interior surrounded by a harder and cooler exterior. As cooling progresses, the interior of the material starts to cool and tries to contract but is constrained by the cooler surface material, causing tensile thermal stresses. As the interior cools further, the surface tensile thermal strains reduce with the development of compressive stress, finally leaving large tensile RS at the core, while compressive RS near the surface. Fig. 6 (a) shows RS distributions in the quenched component for RS in all three directions. The RS in the rolling direction, which contains the largest tensile and compressive stress differences (i.e. $\sigma_z \sim −240$ to 250 MPa) is the main detrimental factor to the part's final dimensional accuracy. The RS in y direction, σ_y, varies from ~0 to 110 MPa, which is much smaller than σ_z due to the shorter transverse dimension of the T-panel. As expected, σ_y approaches ~0 MPa for measurement points close to the surface (i.e. y = 0 mm and y = 24 mm). In terms of σ_x, a similar parabolic distribution was observed compared to σ_z, with smaller magnitudes (i.e. −250 to 127 MPa). These results are similar to the work by Robinson et al. [11], who performed measurements on a 7449 forging. The locations of the peak tensile RS are slightly offset from the centre of the middle line and is at approx. y = 10 mm for σ_z, due to the influence of the web. The uncertainty due to the error in the fitting the peak intensity of the measured RS is around ±30 MPa.

The RS distributions were completely reversed after the T-section panel was subjected to 1.5% CR. As presented in Fig. 6(b), the largest RS distribution exists in the rolling direction (i.e. σ_z up to 268 MPa), while the RS in the other two directions were effectively reduced to within ± 70 MPa. In terms of σ_z, which is of greatest concern, large RS gradients were present within 4 mm of the panel's surface, while a significant decrease was observed in the core of the panel. This re-distributed RS is mainly attributed to the severe shear near the surface and relatively uniform plastic deformations in the core. The type of plastic deformation, created by the cold rolling, relieved most of the central RS from ~250 MPa (i.e. WQ) to ~50 MPa (i.e. WQ + CR), while left high surface RS in the rolling direction. In the aircraft industry, more than ~70% of the material is usually removed by final machining finishing [35]. Therefore, the relatively uniform RS distribution in the interior, which was produced by
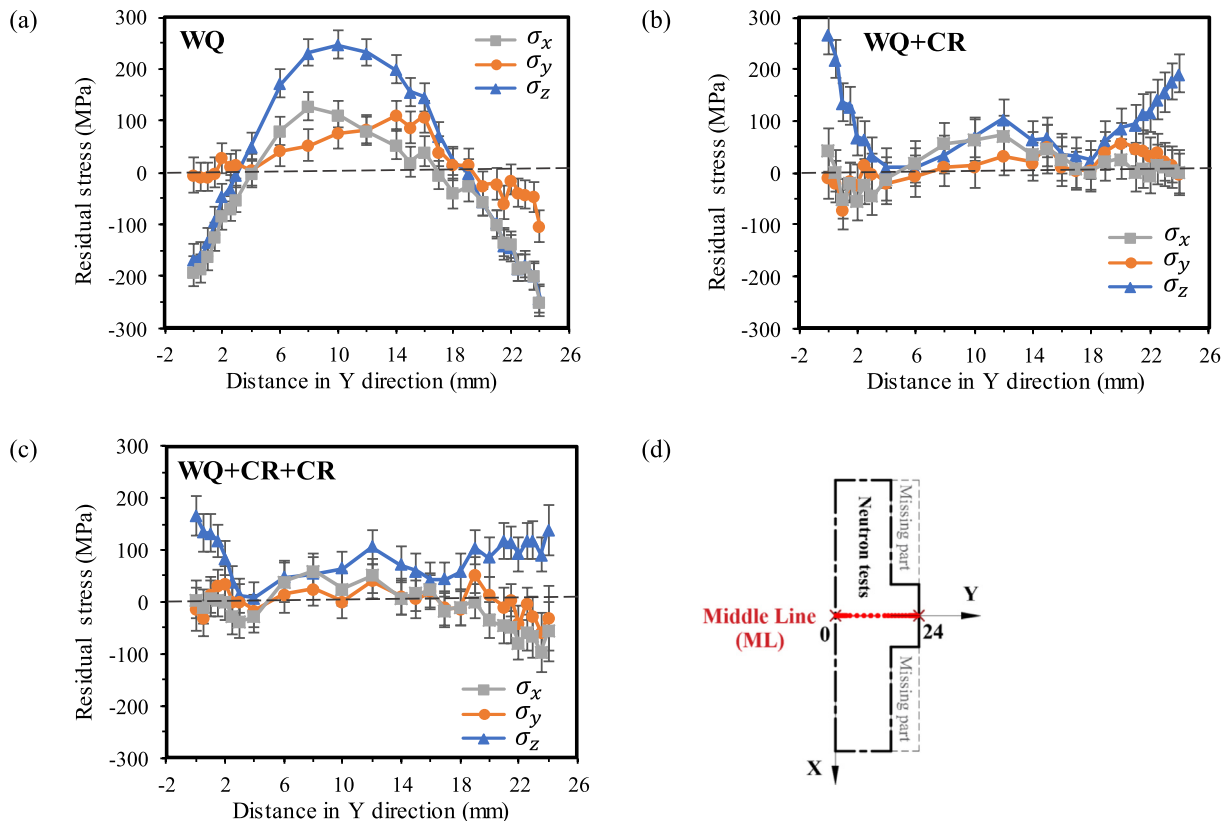

Fig. 6. Residual stress distributions along the middle line of the T-section panels at (a) water-quenched (WQ), (b) cold-rolled (WQ + CR) and (c) constrain-aged (WQ + CR + CA) stages; (d) a schematic illustration of the middle line. The cold rolling level was 1.5%.

cold rolling, is beneficial for the final dimensional accuracy, as large RS regions (i.e. near the surface), which is detrimental to the final dimensional accuracy, will be removed, leaving the interior part with a low and uniform RS distribution. Though the σ_z component of the RS distribution is all tensile and does not self-balanced along the ML (in Fig. 6b), it will be later shown (Fig. 8) that the stress does balance across the full T-cross-sectional area, as required. The uncertainty of the measured RS in WQ + CR is much larger than that of the WQ T-panel, especially near the panel's surface, which is up to ±42 MPa. This can be due to reasons including cold rolling induced texture and dislocation effects. The textures, such as elongated grains and lattice misfits, created by CR, can lead to difficulties in the ND measurements, resulting in a strong variation in intensity of the {311} Bragg peak. Therefore, larger uncertainty of the 2θ values were obtained when using the Gaussian function to fit the intensity and scattering angle relations, hence, resulting in larger uncertainty of calculated RS. Another reason is the partially immersed sample gauge volume by the instrumental gauge volume. Although the average RS of the measurements at 0° and 180° relative to the bisecting angle between incident and diffracted beams, which is explained in more details in Section 2.2, were taken to account for pseudo–strain, the uncertainty induced by the partially buried gauge volume still impact the accuracy of the measurement.

The RS distributions along the ML for the WQ + CR + CA T-panel are shown in Fig. 6(c). After the constrained ageing treatment, the large surface RS (i.e. σ_z) was further reduced to ~100 MPa, while the RS which were initially <~100 MPa were hardly relaxed. To clarify the effects of constrained ageing on the RS reduction in the rolling direction, the RS reduction, $\Delta\sigma_z$, values (i.e. $\Delta\sigma_z = \sigma_{z, wq+cr} - \sigma_{z, wq+cr+ca}$) along the ML of the T-section panel were calculated and plotted in Fig. 7(a). As expected, only the RS on the surface layer (i.e. within 2 mm from the surface) reduced and the maximum reduction (i.e. $\Delta\sigma_z$) was 86 MPa, while no RS reduction (i.e. $\Delta\sigma_z \approx 0$ MPa) was observed from y = 2 to y = 22 mm. The RS reduction by CA is attributed to the thermally activated creep and stress relaxation during ageing at 120°C × 6h + 177°C × 7h. Stress relaxation occurs only if the RS is larger than the threshold stress at the ageing temperature.

To examine the threshold stress of this material for CA, the RS reduction (i.e. $\Delta\sigma_z$) vs. the initial RS (i.e. $\Delta\sigma_{z, wq+cr}$) was presented in Fig. 7(b). It can be concluded that higher RS result in larger RS reductions. However, when the initial RS reduced to ~100 MPa, little or no relaxation in σ_z is observed, which implies that the threshold stress is ~100 MPa for 7050 at the multi-step constrained ageing temperature. According to the experimental SRA behaviour in [35], the plastic deformation history, which induces a large amount of mobile dislocations into the structure, can significantly facilitate the stress relaxation process of 7050 due to both the Orowan's relation (i.e. $\dot{\varepsilon}\propto\rho$) and the promoted precipitation hardening response. Therefore, the larger reduction in the surface RS may also be

attributed to the severe plastic deformation history in the surface region compared to that at the core. Again, the RS uncertainty, receiving from the peak intensity fit, for the WQ + CR + CA part is around ±40 MPa.

Fig. 8 illustrates the residual stress distributions along the side line (SL) of the T-section panels after being treated to water quenching, cold rolling and constrained ageing sequentially, where the squares, circles and triangles represent the RS in X, Y and Z directions, respectively. Typical values of the residual stresses at y = 0 mm, 8 mm, 16 mm for WQ, WQ + CR, WQ + CR + CA T-panels are summarised in Table 3. For the RS distribution in the WQ T-panel, shown in Fig. 8(a), similar RS distributions (i.e. tensile RS in the core while compressive RS near surface) were observed comparing to that along the ML. The measurement uncertainty in the WQ panel was within ±36 MPa. Large σ_x and σ_z were generated by quenching, and their values range from −228 MPa to 146 MPa. While σ_y was generally negligible. The difference between the maximum tensile and compressive RS along SL (i.e. 375 MPa) is much smaller than that along ML (i.e. 493 MPa) due to the smaller thickness (i.e. 16 mm) of the flange part comparing to the web part. Additionally, the peak tensile RS locates in the middle of SL (i.e. y = 8 mm), which implies that the impact of the web on the cooling process of the material along SL are extremely small.

Fig. 8(b) shows the RS distribution after the WQ panel was subjected to 1.5% cold rolling process (WQ + CR). Similar to the ML, the RS distribution after CR on the SL is the reverse of that post WQ of the T-panel (i.e. Fig. 8(a)). σ_x and σ_y were reduced to ~0 MPa, while σ_z exhibits a parabolic profile, with large tensile stresses (i.e. 210 MPa) near the surface while high compressive stresses (i.e. −160 MPa) at the core. Fig. 8 (d) schematically illustrates the locations of the maximum tensile σ_z on the middle (i.e. point A) and side (i.e. point B) line of the WQ T-panel. The maximum tensile σ_z on the ML is 247 MPa, which is ~100 MPa higher than that on the SL (i.e. 146 MPa). After applying the same amount of plastic deformation by the cold rolling, where the point A and B experienced same amount of plastic deformation in the rolling direction, the RS, σ_z, at point B is still smaller than that at point A. The cold rolling modified σ_z at point B should also be smaller than that in the surface region due to the severe surface plastic deformation by CR. Therefore, the σ_z at point B should be the smallest across cross-section area such that: σ_z at point B < σ_z at point A and σ_z at point B < σ_z near surface. To achieve a stress balance over the area, compressive σ_z must exist in the core of the flange parts. The uncertainties of the RS in the WQ + CR T-panel are within ±48 MPa.

Fig. 8(c) illustrates the RS distribution after the T-panel being treated by WQ + CR + CA. In general, the range of the RS values successfully reduced from a range of −160 MPa −210 MPa (before CA) to a range of −71 MPa–130 MPa (i.e. after CA) due to the thermally activated stress relaxation at the ageing temperature. Similar to that along the ML (i.e. Fig. 6 (c)), the RS, which is initially <~100 MPa, hardly relaxed, while the RS at
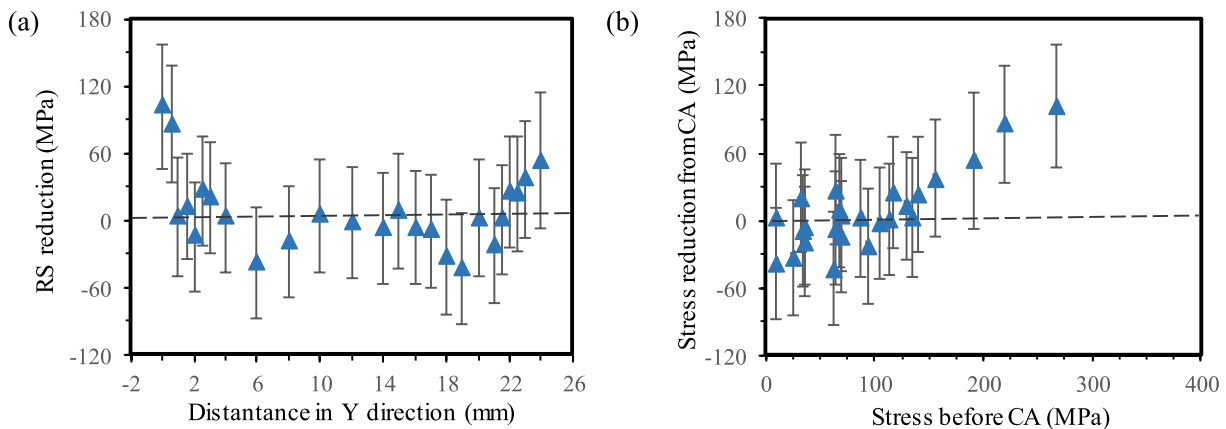

Fig. 7. (a) The residual stress (RS) reduction, $\Delta\sigma_z$, along the ML due to the constrained ageing (CA) treatment; (b) the residual stress reduction, $\Delta\sigma_z$, vs. initial stresses (i.e. the residual stress before CA).
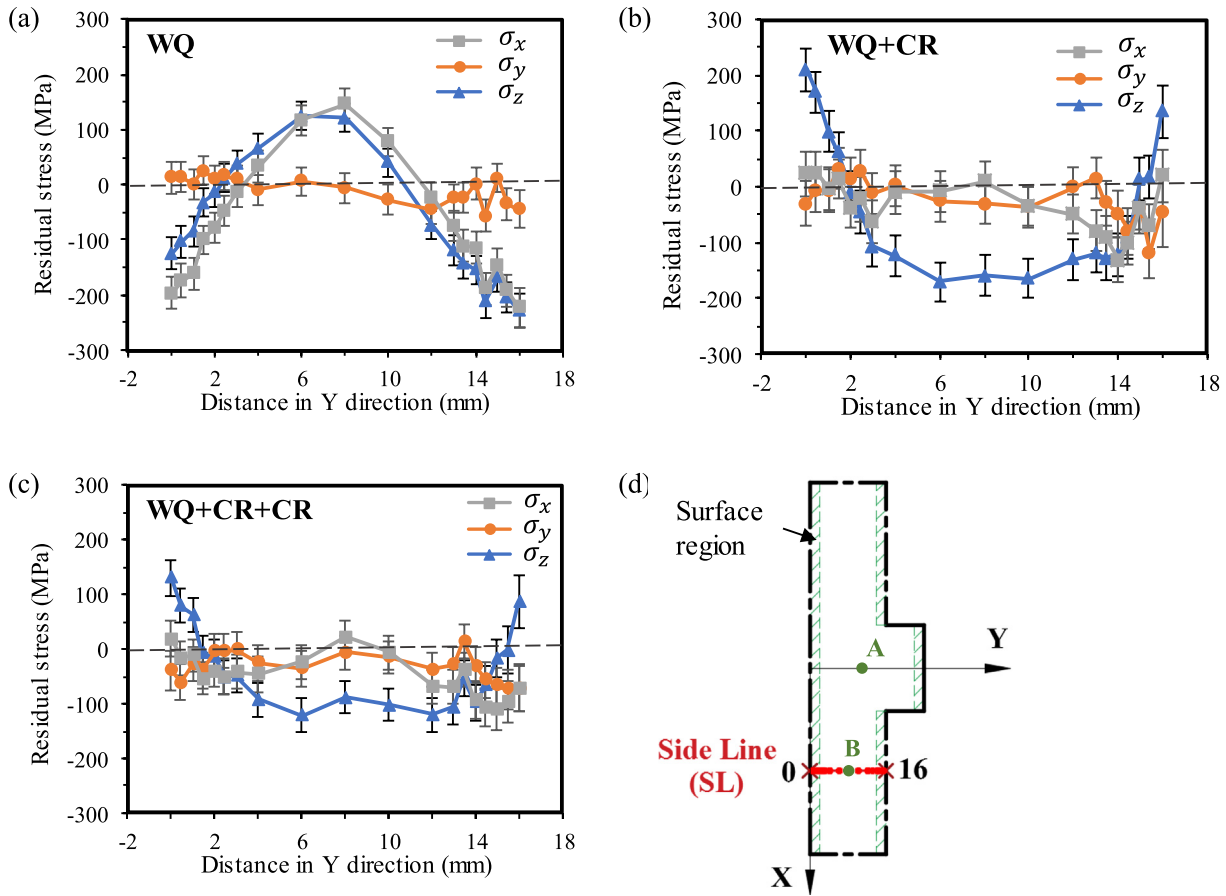
Fig. 8. Residual stress distributions along the side line of the T-section panels at (a) water-quenched (WQ), (b) cold-rolled (WQ + CR) and (c) constrain-aged (WQ + CR + CA) stages; (d) a schematic illustration of the side line and surface region.

the surface and core reduced to ~100 MPa. To clearly present the RS reductions (i.e. $\Delta\sigma_z$) due to CA, $\Delta\sigma_z$ (equals to $\sigma_{z,\ wq+cr} - \sigma_{z,\ wq+cr+ca}$) was plotted against the Y position and against the stresses before CA, as shown in Fig. 9(a) and (b), respectively. As expected, large RS reductions, up to ±80 MPa, were observed at the surface and the core, where the initial RS are higher than ~100 MPa. More importantly, the threshold stress for the stress relaxation process during CA can be determined from Fig. 9 (b). The absolute values of the threshold stresses for tensile and compressive RS relaxations are both ~100 MPa. In addition, no obvious difference was observed in the stress relaxation values for tensile and compressive RS.

The final RS distribution along the SL after the constrained ageing can reflect the RS status in the majority part (i.e. 2 flanges) of the T-panels, which is small in magnitude (~±100 MPa) and flat in the core region (from y = 4–12 mm). It is known that the compressive surface RS benefit the fatigue life of the material, where it reduces the magnitude of tensile stress on the metal surface where cracks initiate and propagate. However, in this case, though large tensile residual stresses were presented in the surface region, these regions will be removed during the final machine finishing, as illustrated in Fig. 10, leaving the core region in service. Therefore, the final RS distribution in this work is suitable for aircraft

application, where only the interior of the panel, containing low and uniform RS distributions, is left.

The σ_z at the web surface (i.e. X = 0 mm and 24 mm) and the flange surface (X = 0 mm and 16 mm), which are located at the same positions as the ND measurements along the ML and SL (i.e. in Fig. 2(b)), respectively, were selected and plotted together with the ND measured σ_z in Fig. 11, for the cold rolling levels of 1.5%. The yellow circles, blue squares and red triangles represents the measured residual stresses at the WQ, WQ + CR(1.5%) and WQ + CR(1.5%) + CA stage, respectively, where solid symbols are ND measured RS and hollowed symbols are XRD measured RS values. As can be seen, the XRD measured surface RS agrees well with the ND measured RS at each processing stages, therefore, confirmed the reliability of the measured RS distributions.

3.3. Deflections and hardness distributions at each stage

Fig. 12 presents the deflections in the Z direction of the quenched T-section panels after being quenched (WQ), cold rolled (WQ + CR) and subsequent constrained aged (WQ + CR + CA). The cold rolling levels are 1.5% and 3.0%. In general, the T-section panel retained flat after WQ, where the heights of the flange at various Z locations are all

Table 3
The residual stress values for WQ, WQ + CR, WQ + CR + CA T-section panels at Y = 0, 8 and 16 mm.

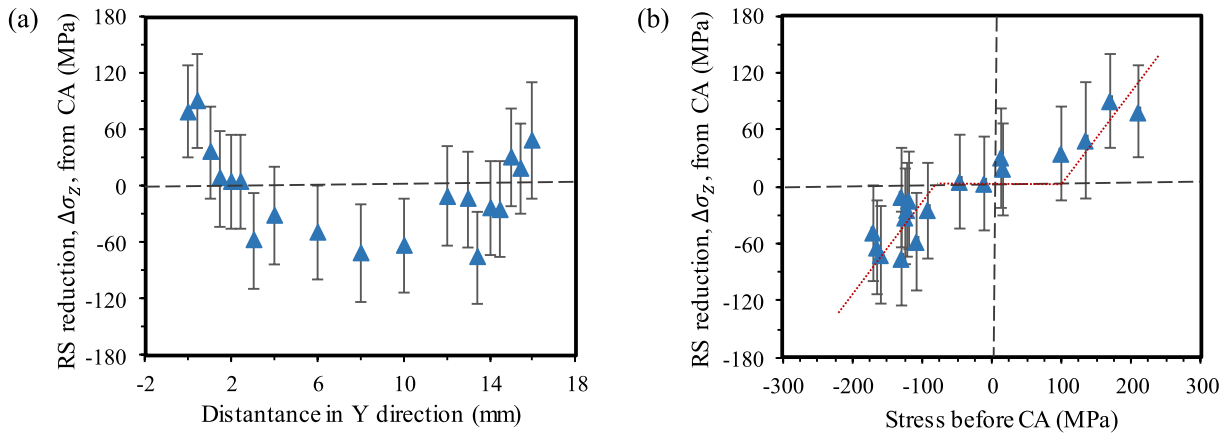| Y (mm)	WQ			WQ + CR			WQ + CR + CA		
	Y = 0	Y = 8	Y = 16	Y = 0	Y = 8	Y = 16	Y = 0	Y = 8	Y = 16
σ_x (MPa)	−195.79	146.44	−222.76	24.10	9.14	20.28	18.70	22.54	−71.38
σ_y (MPa)	13.212	−5.16	44.52	−30.43	−30.27	−65.78	−38.89	−5.89	−65.78
σ_z (MPa)	−124.00	121.75	−228.54	210.03	−160.15	134.81	130.80	−88.80	86.20

Fig. 9. (a) The RS reduction, $\Delta\sigma_z$, along the SL due to the CA treatment; (b) the RS reduction, $\Delta\sigma_z$, vs. initial stresses (i.e. RS before CA).

~16 mm. The flat T-panels were curved toward the convex surface after the cold rolling treatment for both levels: 1.5% and 3.0%. The curved deflections are attributed to the different exit velocities of the top (i.e. convex) surface and the bottom (i.e. flat) surface during the cold rolling. Though given the same angular velocity to the two rollers during cold rolling, the line velocities of them still exhibit slight difference due to the different shape of the rollers. The diameter of the groove region on the grooved roller is 16 mm smaller than that of any other regions on the two rollers. Therefore, the convex surface generated smaller exit velocities than that of the flat surface, resulting in a strain gradient through the part's thickness and thus leading to bending. Comparing the deflections before and after the constrained ageing, though a small difference in the T-panel's curvature is expected due to the RS redistribution after CA, negligible difference was observed for both 1.5% CR (i.e. Fig. 12(a)) and 3.0% CR (Fig. 12(b)). The unchanged deflections imply that the RS relaxation during CA did not leave a large and unbalanced moment on the cross-sectional area of the T-panel, and thus leading to a minor change in the T-panel's curvature. Comparing the deflections created by the cold rolling of 1.5% and 3.0%, larger values, up to 37 mm in height, were observed of the T-panel after CR 3.0% than that, ~30 mm, after CR 1.5%.

Fig. 13 illustrates the hardness distribution (a) cross the web (i.e. ML) and (b) flange (i.e. SL) thicknesses of T-section panels, where circular, square and triangle represent the hardness values at WQ, WQ + CR and WQ + CR + CA stage, respectively. The average hardness of the WQed T-panels are 148 HV10 and no obvious trends were observed both along the ML and SL, which indicates that quenching generated a homogenous Super Saturated Solid Solution (SSSS) in the structure. This hardness value is similar to the results from Tanner, et al. [37], who examined the precipitation evolution for W-temper 7010 during natural ageing. For the WQ + CR T-sections, an average hardness of 155 HV10 was obtained. The increase in the hardness value is due to the work hardening effects created by the cold rolling process. Dislocations are expected to be created by CR and the amount of dislocation is in positive correlation with the deformation levels, neglecting any static recovery at room temperature. During rolling, more dislocations were created near the surface while less dislocations in the core, resulting in a higher hardness value (i.e. ~160 HV10) at the surface while a relatively
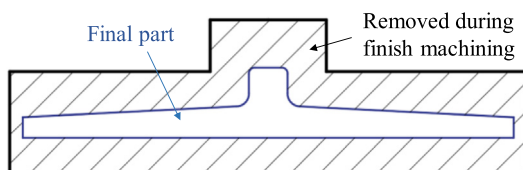
low value (i.e. ~150 HV10) in the centre for the hardness both along ML and SL. After constrained ageing, over-aged T-panels were obtained with an average hardness value of ~157 HV10.

In terms of the final hardness values after the whole manufacture process (i.e. WQ + CR + CA), as shown in Fig. 13(a), a lower hardness (i.e. ~155 HV10) exsists near the surface, while high hardness values (i.e. ~163 HV10) exist in the core. This phenomenon indicates that the near surface precipitation in CA was enhanced by the surface dislocations both generated from the cold rolling and from the stress relaxation, leading to a more severe over-aged state than that in the core. There are two reasons for the enhancement: firstly is the coarser precipitates formed on and around dislocations. A large amount of dislocations was formed in the surface region. These dislocations are low energy sites that are favour for the nucleation and growth of the precipitates. Given the certain over-ageing time (i.e. 14 h), precipitates were rapidly formed on dislocations by a competitive growth, absorbing more Zn, Mg, etc., elements in the Al matrix and resulting in smaller precipitate quantities while larger precipitate sizes [35] in the surface region. These larger precipitates reduced the ability to hinder further dislocation movement and thus leading to a decreased hardness near the surface. The second reason is the unevenness of the precipitate distributions near the surface. The amount of dislocations can also modify the precipitate distribution, leaving larger precipitates on dislocations, precipitate free zones near dislocations and smaller precipitates in the Al bulk matrix. This unevenness in the precipitate distribution can also reduce the part's hardness near the surface. Based on the understanding of the dislocation effects on the precipitation process, one can conclude that the weakest parts (i.e. low hardness and strength regions) of the T-panels should be the place where large residual stress were initially created by the cold rolling process. This is because high residual stress region (i.e. Y = 0–2, 22–24 mm in Fig. 6(c)) relaxed more during CA (i.e. Fig. 7) and created more dislocations due to the thermally activated creep. In addition, the effect of the CR induced plastic deformation should also be considered. Fig. 13(b) gives the hardness distribution along the SL. In terms of the final hardness distribution (i.e. WQ + CR + CA), as explained and expected, slightly lower hardness values (i.e. ~160 HV10) were observed in both the surface region and centre region, which is attributed to the higher residual stresses in both the surface and the core. In addition, the large plastic deformation near the surface should also contribute to the lower surface hardness, but the contribution may not be comparable to that of the residual stresses, according to Zheng, et al. [35]. From final hardness (i.e. WQ + CR + CA) distributions along ML and SL, though the hardness values vary and in surface regions are slightly smaller than the standard T74 hardness value (i.e. ~162 HV), they still can meet the industrial requirement, where only the core region will be left for service after the machine finishing.
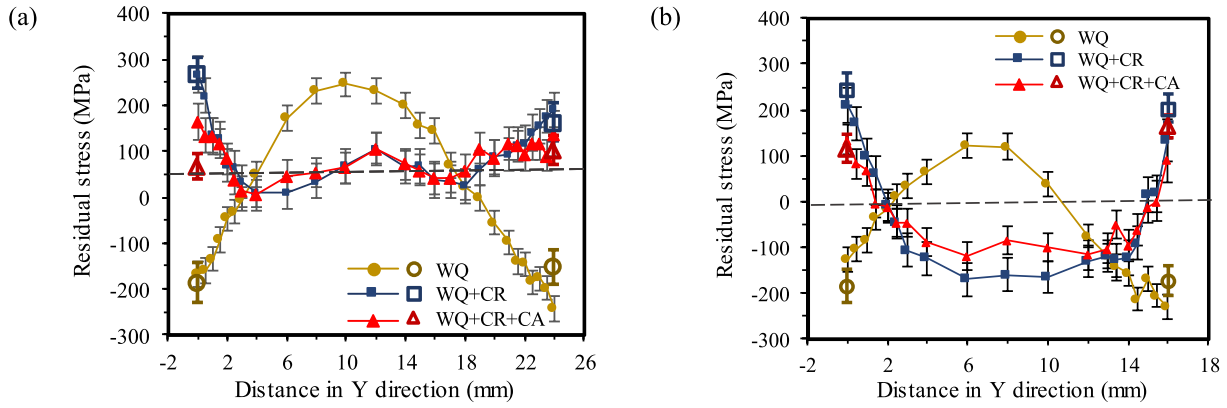

Fig. 10. Schematic illustration of the final part after finish machining the T-section panel.

Fig. 11. Comparison between the neutron diffraction measured (solid symbols) and the X-ray diffraction measured (hollowed symbols) residual stresses along the (a) middle line and (b) side line of the T-section panels at WQ, WQ + CR and WQ + CR + CA stages. The cold rolling level was 1.5%.

4. FE modelling of the water quenching (WQ), cold rolling (CR) and constrained ageing (CA) processes

4.1. Material property modelling

In order to build appropriate FE models to simulate the water quenching, cold rolling and constrained ageing process, two separate user material (VUMAT) subroutines were employed in the FE simulation, one for WQ and CR and the other for CA. The constitutive equations employed in these two subroutines were established and validated using uniaxial compression and stress relaxation ageing uniaxial test results, where the detailed determination of the equations can be found in [33,38].

The first subroutine's corresponding constitutive equations are shown in Table 4. This set of equations were used to predict the RS generation by quenching and RS reduction by cold rolling. The constitutive equations have been validated using the uniaxial compressive tests data at different temperatures (i.e. ranging from 20 to 450 °C) and different strain rate (i.e. from 0.01 to 1s⁻¹). The detailed explanation of the set of equations can be found in [33] and a brief explanation of each parameters and material constants are given in Table 4.

The constitutive relations incorporated into the subroutine to simulate constrained ageing process are given in Table 5. The set of constitutive equations were developed based on the interactions between the dynamic precipitation hardening and the stress relaxation curves at each constant strain levels. The pre-strain effects on the strength and stress relaxation behaviours were also incorporated. The set of material constants list in Table 5 have been calibrated by uniaxial stress relaxation ageing tests at different initial stresses and post different pre-strain levels (0–3%). Detailed derivations of these equations and the determination of these material constants can be found in [33].

In the VUMAT, the equivalent stress was initially calculated according to the von Mises yield criterion in Eq. (4). While the plastic flow rule was adopted at the end to split the equivalent plastic strain rate, $\dot{\varepsilon}_{eq}^p$, to normal and shear strain rates in x, y, z directions, such that Eq. (5) is satisfied:

$$\sigma_{eq} = \sqrt{\frac{3}{2} S_{ij} : S_{ij}} \tag{4}$$

$$\dot{\varepsilon}_{ij}^c = \frac{3}{2} \frac{S_{ij}}{\sigma_{eq}} \dot{\varepsilon}_{eq}^c \tag{5}$$

where S_{ij} is the stress deviator tensor, $\sigma_{ij} - \frac{1}{3}\sigma_{kk}$, σ_{eq} is the equivalent stress $\dot{\varepsilon}_{eq}^c$ is the equivalent plastic strain rate and $\dot{\varepsilon}_{ij}^c$ is the plastic strain rate tensor.

4.2. Finite Element Model

A half model of the T-section panel was built using ABAQUS CAE employing symmetry conditions, as illustrated in Fig. 14. 3D 8 noded diffusive heat transfer elements (DC3D8) were employed for the WQ analysis while 3D continuum 8 noded elements with reduced integration
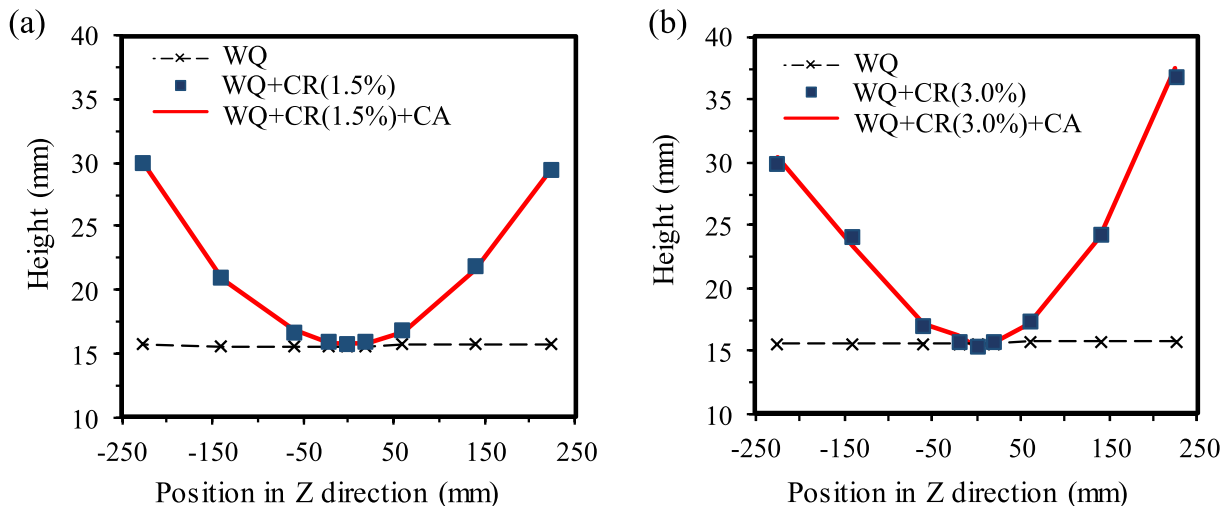

Fig. 12. Comparison of the surface profiles at each processing stage. The cold rolling levels were (a) 1.5% and (b) 3.0%.
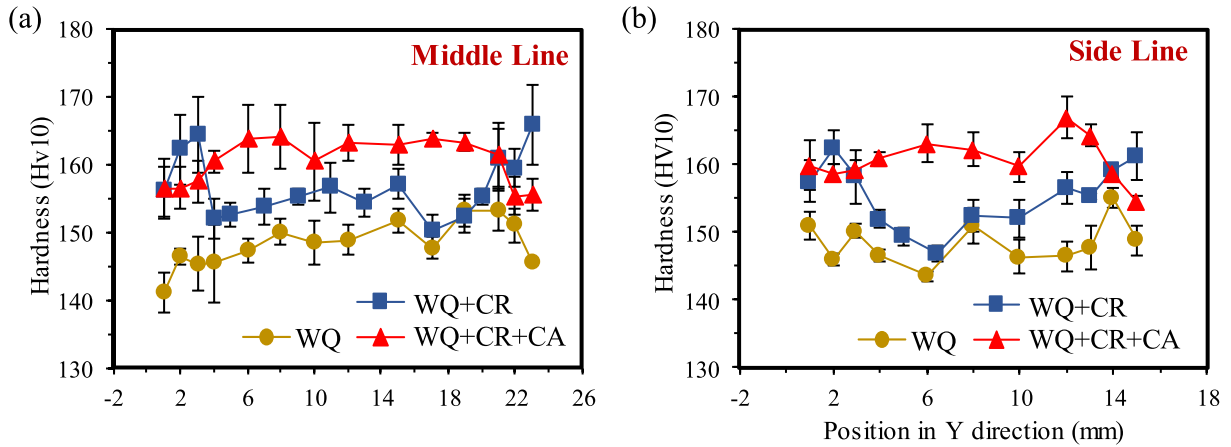
Fig. 13. The Vickers hardness along the (a) middle line and the (b) side line of the T-section panels at water-quenched (WQ), cold-rolled (WQ + CR) and constrain-aged (WQ + CR + CA) stages. The cold rolling level is 1.5%.

points (C3D8R) were employed for the CR and CA analyses. The element size was $1.5 \times 1.5 \times 1.5$ mm. Given the T-section dimensions, a total of 100,500 elements were used.

For the WQ FE simulation, a sequentially thermal-mechanical analysis was performed, where the heat generation from plasticity during quenching is considered negligible. Two types of elements, DC3D8 and C3D8R, were employed for thermal and mechanical analysis, respectively, during quenching. The abovementioned user-defined subroutine was used for the mechanical analysis. Both radiation and convection heat transfer boundary conditions were applied. The analysis was divided into three steps: (i) air cooling (5 s), where the convection heat transfer coefficient in air was taken to be 10 W/m^{2}K; (ii) lowering period (0.8 s), counting from the T-section panel started to contact with water to fully immersed into water; (iii) water cooling, where the convection heat transfer coefficient was collected from [38,39]. The temperature of the T-section panel was initially set to 475 °C, which is the SHT temperature, while the ambient temperature was taken as 20 °C. Other temperature-dependent thermal parameters, e.g. thermal conductivity, density and specific heat, were taken from Baldwin et al. [90]. The quenching direction was set in the transverse direction, as shown in Fig. 14.

For the FE simulation of CR, two rollers were modelled: one with a flat surface while the other had a groove in the middle. The dimensions of the rollers were identical to that of the rollers used in experiments. The thickness reduction of the T-section panel can be controlled by adjusting the distance between the two rollers. The rolling angular velocity was taken to be 1 rad/s according to the laboratory conditions. An assumption was made that the stiffness and strength of the rollers were sufficiently large so that negligible deformations occurred on the rollers during CA. Thus an 'analytical rigid body' was used for the two rollers. The CR analysis was divided into two steps: (i) the T-section panel was pushed toward the roll gap with a constant velocity of 2 mm/s, until contacting the rollers; (ii) the T-section was rolled, and its movement is determined by the friction force provided by the rollers. The friction coefficient between the rollers and the T-panel was 0.1 [40]. The element type for CR was 3D solid continuum 8 noded with reduced integration points (C3D8R). The user-defined subroutine, specifically the stress-strain curve at room temperature, was used in the CR-model. Due to the relatively small plastic deformation in CR, the heat generation from plastic deformation was neglected.

For the FE simulation of CA, the deformed configuration of the CR-model was imported into the constrained ageing model (CR-model).

Table 4
Constitutive equations employed in the WQ and CR model's subroutine for as-quenched 7050 at different temperatures with different strain rates.

Constitutive equations	Temperature dependent constants	Material constants
$\dot{\varepsilon}^p_{eq} = \left\lvert \dfrac{\sigma_{eq} - H - \sigma_{ys}}{K} \right\rvert^{n1}$ $\dot{\bar{\rho}} = A(1-\bar{\rho})\lvert\dot{\varepsilon}^p_{eq}\rvert - C_1\bar{\rho}^{n2}$ $H = B\sqrt{\bar{\rho}}$ $\dot{\varepsilon}^p_{ij} = \dfrac{3}{2}\dfrac{S_{ij}}{\sigma_{eq}}\dot{\varepsilon}^p_{eq}$ $\sigma_{ij} = E(\varepsilon^T_{ij} - \varepsilon^p_{ij})$	$K = K_0 \cdot exp(\dfrac{Q_K}{RT})$; $C_1 = C_{1,0} \cdot exp(\dfrac{-Q_{C_1}}{RT})$ $n_1 = n_{1,0} \cdot exp(\dfrac{Q_{n_1}}{RT})$; $\sigma_{ys} = \dfrac{\sigma_{y_0}}{cosh^2(\alpha_k(T-T_0))}$; $B = \dfrac{B_0}{cosh^2(\alpha_B(T-T_0))}$; $E = E_0 \cdot exp(\dfrac{-Q_E}{RT})$; Q_K, Q_{C_1}, Q_{n_1}: activation energies $K_0, C_{1,0}, n_{1,0}, k_0, B_0, \alpha_k, \alpha_B$: material constants R: the universal gas constant T: temperature	$A = 15.62$ (−); $n_2 = 1.60$ (−); $\sigma_{y_0} = 166.12$ (MPa); $\alpha_k = 4.11e-3$ (°C^{-1}); $K_0 = 13.11$ (MPa); $Q_K = 4.11e3$ (J/mol); $n_{1,0} = 0.69$ (−); $C_0 = 2.99e5$ (s^{-1}); $Q_c = 5.88e4$ (J/mol); $B_0 = 255.00$ (MPa); $\alpha_B = 3.00e-3$ (°C^{-1}); $E_0 = 3.13e4$ (MPa); $Q_E = 795.24$ (J/mol); $Q_{n_1} = 6.81e3$ (J/mol);

ε^p_{eq}: equivalent plastic strain
σ_{eq}: equivalent stress
H: hardening parameter
σ_{ys}: yield stress
K: drag stress
n_1: stress exponent
$\bar{\rho}$: normalised dislocation density
ε^T_{ij}: total strain tensor
ε^p_{ij}: plastic strain tensor
σ_{ij}: stress tensor
A, C_1, n_2, B: material constants
Detailed explanation refer to [25]

Table 5

Constitutive equations and yield strength evolution expressions employed in the constrained ageing model's subroutine relation for 7050 during constrained ageing with different pre-strain levels.

Constitutive equations & temperature dependent constants	Material constants
$\dot{\varepsilon}^p_{eq} = A_s\left(\dfrac{\sigma_{eq} - k\sigma_{ys}}{\sigma_0}\right)^{n(1+\bar{\rho})}$; $\sigma_{ys} = \sigma_{solute} + \sqrt{\sigma^2_{ppt} + \sigma^2_{dis}}$; $\dot{\sigma}_r = C_r \bar{r}^{m_2}(1-\bar{r})$; $\sigma_{ppt} = \sigma_r \cdot \bar{f}^{m_1}$; $\sigma_{solute} = C_{ss}(1 - B_{ss}\bar{f})^{m_3}$; $\sigma_{dis} = A_{ds}\bar{\rho}^{m_4}$; $\dot{\bar{r}} = A_r\{ \exp(-\dfrac{Q_v}{RT}) + a_c[1 - \exp(-\alpha_1 \bar{r})]\exp(-\dfrac{Q_c}{RT})\bar{\rho}^{m_r}\}(\bar{R}_{max} - \bar{r})^{m_{r_1}}$; $\dot{\bar{f}} = A_f \cdot (1-\bar{f}) \cdot \dot{\bar{r}} \cdot \bar{r}^2$; $\dot{\bar{\rho}} = A_d(1-\bar{\rho})|\dot{\varepsilon}^p_{eq}| - C_d \bar{\rho}^{m_5}$; $\bar{R}_{max} = \bar{R}_{max_0} \cdot \exp(-\dfrac{Q_v}{RT})$; $C_d = C_{d_0} \cdot \exp(-\dfrac{Q}{RT})$; $A_s = A_{s_0} \cdot \exp(-\dfrac{Q}{RT})$; $k = k_0 \cdot \exp(\dfrac{Q}{RT})$ $\dot{\varepsilon}^p_{eq}$: equivalent creep strain σ_{eq}: equivalent stress σ_{ys}: yield strength σ_r: precipitate radius contributed strength σ_{ppt}: precipitate contributed strength σ_{solute}: solid solute contributed strength σ_{dis}: dislocation contributed strength $\bar{r}$: normalised precipitate radius $\bar{f}$: normalised precipitate volume fraction $\bar{\rho}$: normalised dislocation density $A_s, \sigma_0, n, C_r, m_2, m_1, m_3$, etc. are material constants (detailed explanation refer to [38]) Q_v, Q: activation energies relate to precipitate formation and precipitate-dislocation interaction $\bar{R}_{max_0}, C_{d_0}, A_{s_0}, k_0$: material constants R: the universal gas constant T: temperature	$n = 1.75\ (-)$; $m_1 = 0.18\ (-)$; $C_r = 1100.00\ (\mathrm{h}^{-1})$; $m_2 = 1.00\ (-)$; $C_{ss} = 247.00\ (\mathrm{MPa})$; $B_{ss} = 0.60\ (-)$; $m_3 = 0.67\ (-)$; $A_{ds} = 95.00\ (\mathrm{MPa})$; $m_4 = 0.77\ (-)$; $A_r = 0.04\ (\mathrm{h}^{-1})$; $a_c = 1.05e4\ (-)$; $\alpha_1 = 25.32\ (-)$; $m_{r_1} = 1.00\ (-)$; $m_r = 2.00\ (-)$; $A_f = 12.16\ (-)$; $A_d = 37.62\ (-)$; $m_5 = 2.58\ (-)$; $A_{s_0} = 0.30\ (\mathrm{h}^{-1})$; $k_0 = 4.50e-4\ (-)$; $C_{d_0} = 837.21\ (\mathrm{h}^{-1})$; $\bar{R}_{max_0} = 1170.00\ (-)$; $Q = 23.19\ (\mathrm{kJ/mol})$; $Q_v = 24.67\ (\mathrm{kJ/mol})$; $Q_c = 13.00\ (\mathrm{kJ/mol})$; $\sigma_0 = 1.00\ (\mathrm{MPa})$; $C_{d_0} = 837.21\ (\mathrm{h}^{-1})$;

In addition, the predicted RS and plastic strain values for each element were assigned as pre-defined fields to the CA-model. Boundary conditions were applied to fix the part's displacements in the y coordinate direction during constrained ageing, while the relaxed residual stresses were calculated using the CA subroutine, detailed in Table 5. After CA, the fixed displacement boundary condition was released.

4.3. Prediction of the RS distribution at each stage of the manufacturing process

The residual stress predictions are compared to the experimental residual in Fig. 15 along the middle line (ML) (a, d and g) and side line (b, e, h) and of the T-section panels at each stage of the manufacturing process. The black, orange and blue colours in Fig. 15(a, b, d, e, g, h) represent the RS in x, y and z direction, respectively, where symbols are experimental results and solid lines are predicted results. As can be seen, excellent agreement was achieved in all three directions (x, y, z) at all stages, except for some underestimation of the residual stresses for WQ T-panel along the SL. The under prediction of the quenched RS along SL may be attributed to errors in the heat transfer coefficients. Fig. 15(c), (f) and (i) shows a contour plot of the predicted residual stress distributions at each processing stage in the rolling direction (i.e. σ_z) on the central cross-sectional area. As expected, WQ induced a large tensile RS in the core and the RS value decreases layer by layer until approaching the part's surface. For the predicted σ_z map of the WQ + CR T-panel, large tensile σ_z stresses are present at the surface, while large compressive σ_z (i.e. up to -180 MPa) in the core of the flange region. As previously discussed, this distribution is attributed to the non-uniform plastic deformation created on the surface layer by CR and the previous σ_z distribution
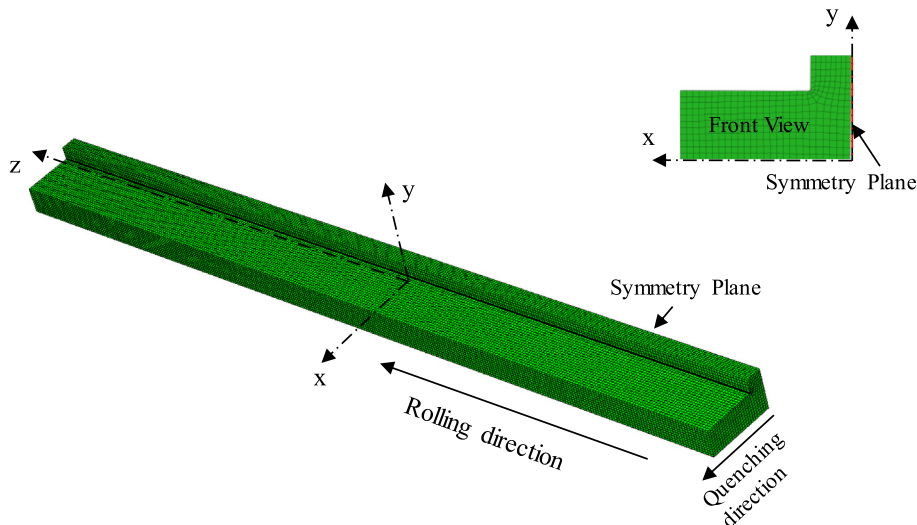

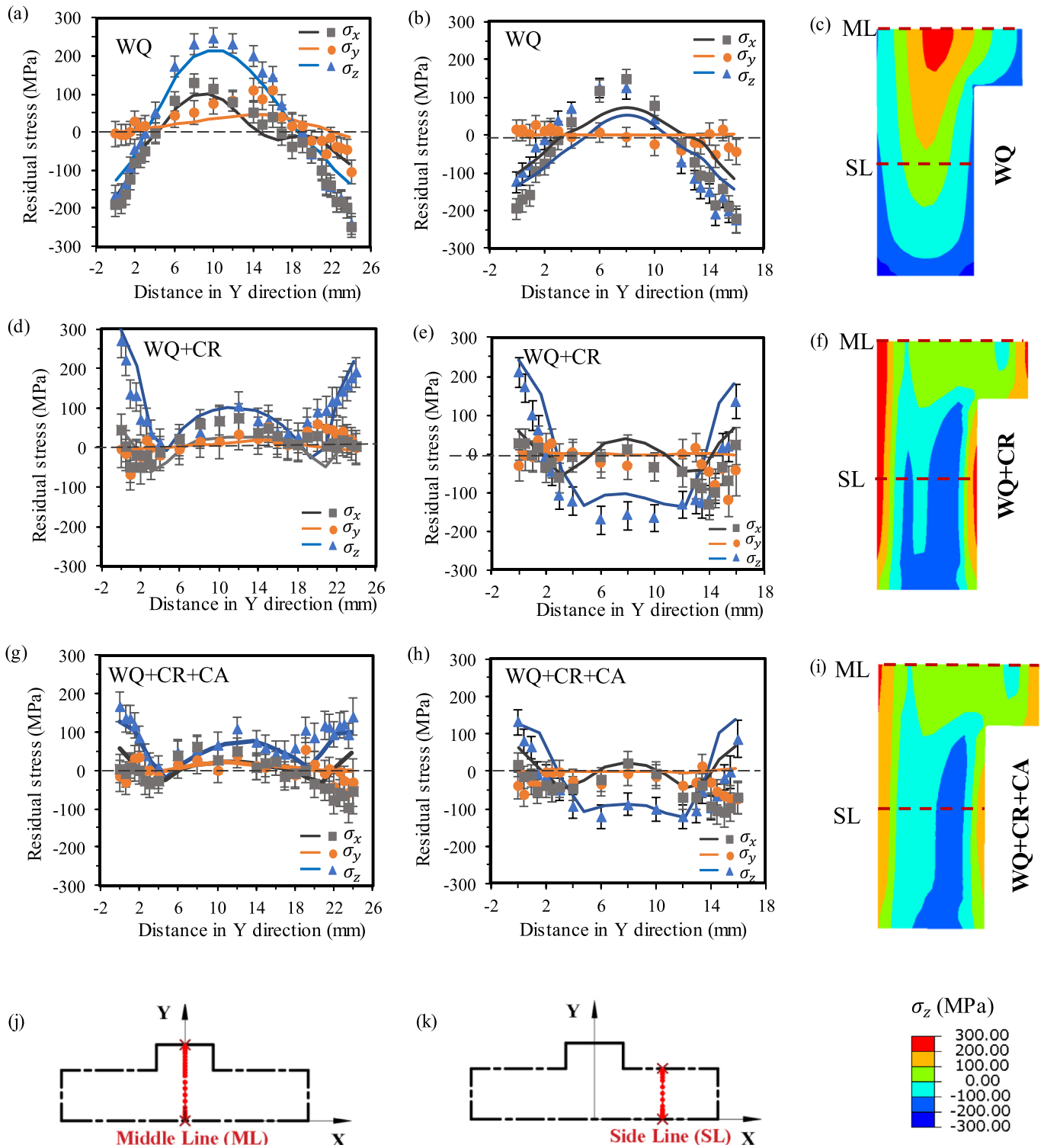**Fig. 14.** Illustration of the finite element mesh, symmetry plane and coordinates.

Fig. 15. The experimental (symbols) and predicted (solid line) residual stresses (i.e. σ_x, σ_y, σ_z) along (a), (d), (g) the middle line (ML) and (b), (e), (h) the side line (SL) of the T-section panels at water quenched (WQ), cold rolled (WQ + CR) and constrained aged (WQ + CR + CA) stages; (j), (k) schematic illustrations of the ML and SL. (c), (f), (i) The FE predicted σ_z distributions at each stage.

induced by WQ. Detailed explanation has been given in Section 3.2.2 and Fig. 8. After the T-panel was finally subjected to constrained ageing, the large surface residual stress and the large core residual stresses, which initially had magnitudes larger than ~100 MPa, further reduced to within ~100 MPa, while those residual stresses, less than ~100 MPa, showed little change. Fig. 15(i) gives the predicted final σ_z distribution, which is as expected.

4.4. Prediction of micro-structural internal variables and the yield strength

The final hardness values (i.e. post the whole manufacture process: WQ + CR + CA) were converted to a yield strength value, σ_{YS}, using the hardness-strength relationships in [41], i.e. Eq. (6)

$$\sigma_{YS} = 3.756 Hv - 188.5 \qquad (6)$$

where H_v is the Vickers hardness value. The calculated σ_{YS} are plotted together with the predicted yield strength along the ML and SL in Fig. 16. As illustrated in Fig. 16(a) and (b), though a slight under prediction of the yield strength values (i.e. the predicted average σ_{YS} is ~8 MPa lower than the converted σ_{YS}) was observed, the predicted curves still give reasonable trends compared to that of the converted yield strength values, where lower σ_{YS} exist near the surface while higher σ_{YS} are present in the core region. This is attributed to the large amount of dislocations in the surface region, which significantly enhanced the ageing progress, leading to lower surface yield strengths. Fig. 16(c) shows the predicted yield strength distribution over the T-cross sectional area. As can be seen, the highest yield strength (i.e. up to ~418 MPa) are present in the core region, while the lowest yield strength (i.e. ~377 MPa) are predicted on the web's surface. As discussed in Section 3.3, the severe over-ageing area is attributed to the CR and CA induced dislocations.

Fig. 17 illustrates the final distributions of the two internal state variables (i.e. the normalised precipitate radius, $\bar{r}$, and normalised precipitate volume fraction, $\bar{r}$), calculated from the constitutive equations in Table 5. Note that the set of constitutive equations were taken from [38], where the internal state variables were physically based and have been experimentally validated using the TEM tests. Although these internal state variables cannot directly represent the precipitate distributions at a microscopic scale, they are microstructural related variables that indicate the overall distribution trends of the precipitate radius and volume fractions. Fig. 17(a) illustrates the predicted normalised precipitate radius, $\bar{r} = \frac{r}{r_{peak}}$, after CA, where r and r_{peak} are the current precipitate radius and the precipitate radius at the peak aged state (~5 nm [3,42]), respectively. Similar conclusions to the yield stress predictions can be made (as shown in Fig. 16), i.e. a severe over-aged region with larger precipitate sizes exists at the surface. The precipitate size was around 1.5 times r_{peak}, which is consistent with the experimental observations in [35]. Fig. 17(b) presents the predicted normalised precipitate volume fraction, $\bar{f} = \frac{f}{f_e}$, where f_e is the equilibrium precipitate volume fraction at a certain temperature. After the over-ageing treatments, all elements, e.g. Zn, Mg, are expected to be depleted from the Al matrix, which is also an assumption in the constitutive equations [38]. Thus, the values of the $\bar{f}$ at all locations are all around unity, thus their contributions to the material's yield strength are uniform throughout the part.

4.5. The predicted RS in the rolling direction (σ_y) and the yield strength (σ_{ys}) evolutions during CA

The predicted evolution of the residual stress distributions (i.e. in the rolling direction) and the corresponding yield strength distributions, at the start ($t = 0.00$ h), peak ageing time (7.63 h), 12.95 h and at the end (14 h), of CA are shown in Fig. 18. It can be concluded that the most efficient period for RS reduction during CA is from $t = 7.63$–12.95 h, where the majority of the large surface residual stresses (approx. $\pm$ 200 MPa) reduce to around $\pm$100 MPa. The residual stress shows little reduction at $t = 0.00$–7.00 h, due to the relatively low ageing temperature (i.e. 120 °C) which is insufficient for significant creep to occur [35]. Similarly, RS hardly reduces from $t = 12.95$ to 14 h, as the RS magnitudes at $t = 12.95$ h are smaller than the 7050 threshold stress (i.e. ~100 MPa). Therefore, no further reduction in RS can be achieved. In terms of the predicted yield strength evolution, the yield strength increases from $t = 0.00$ h (under-age), reaching its peak (i.e. ~555 MPa) at $t = 7.63$ h, and then decreases to ~400 MPa at $t = 14$ h (over-age). By a detailed examination of the RS and yield strength evolution, it can be concluded that $t = 12.95$ h is most appropriate for the CA treatment to produce the T-section panel with target material properties and residual stress levels, where most of the T-section contained residual stresses to within $\pm$100 MPa, while maintaining a yield strength higher than 412 MPa. However, reducing the ageing time may affect stress corrosion cracking properties of the final T-panel [26]. Therefore, an examination on the stress corrosion cracking properties of the T-panel is necessary, and thus is recommended for future work, to guarantee the overall property of the final T-panel if the CA time is reduced.

5. Discussion

5.1. RS distribution by CR

It was observed that the residual stresses generated by quenching (a parabolic profile from −300 MPa to 300 MPa) were completely reversed by cold rolling with large tensile RS (~$\pm$200 MPa) at the surface and compressive RS at the core. At present, industry performs a multi-step compression technique to reduce residual stresses, where a small-sized mould is used to sequentially compress the length of the part to achieve the required plastic deformation. Though cold compression has
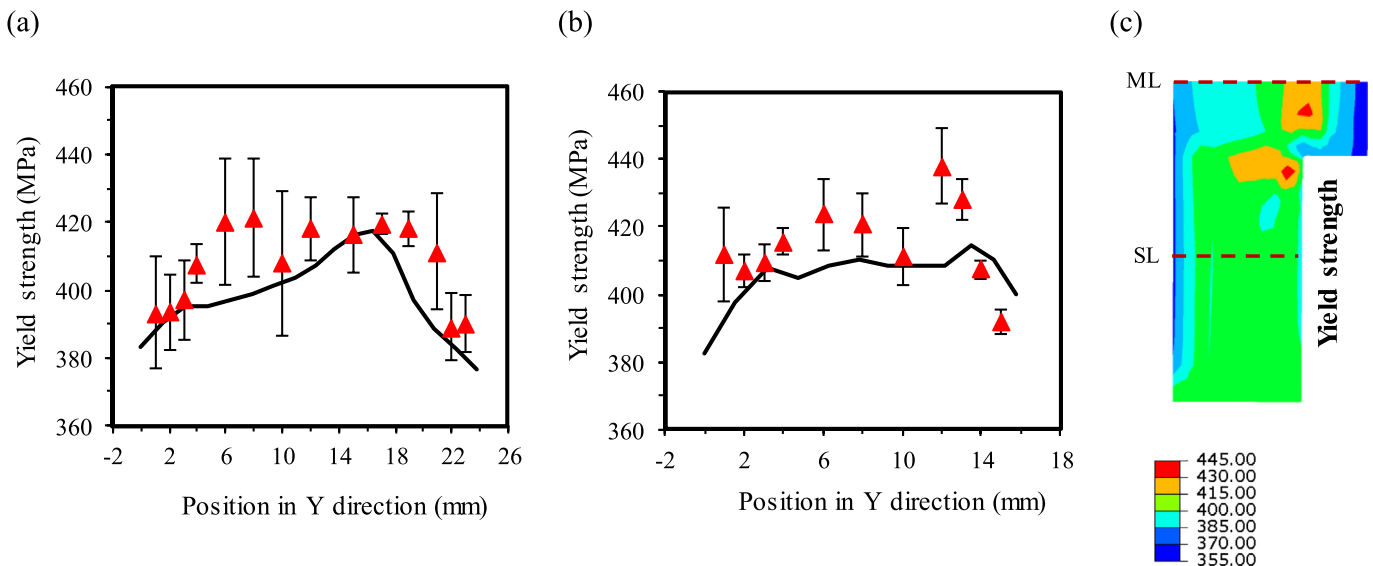

Fig. 16. The experimental (symbols) and predicted (solid line) yield strength along the (a) middle line and (b) side line of the T-section panels after the final constrained ageing treatment. (c) The FE predicted yield strength distribution. Note that the experimental yield strength is calculated using the hardness-strength formula in [41].
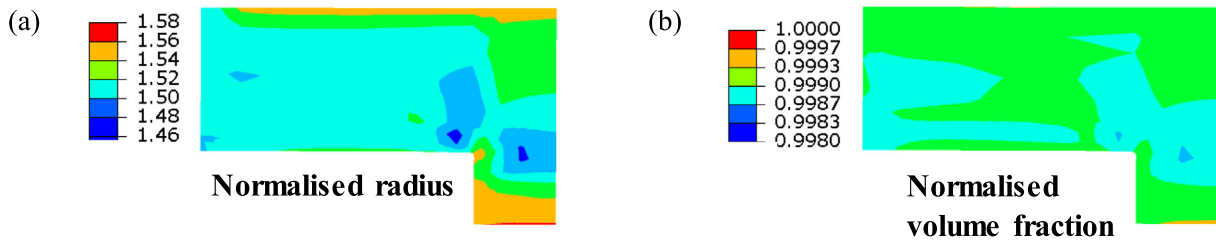
Fig. 17. The predicted (a) normalised precipitate radius and (b) normalised precipitate volume fraction after the constrained ageing treatment.

shown its effectiveness in significant reducing RS levels to <100 MPa for simple geometry components, as reported in [11,23,43], multi-step compression causes significant issues. According to the multiple compression simulations performed by Pan et al. [25] and the on-going issues with distortion concerning the aircraft industry, results showed that uncontrollable and non-repeatable RS distributions were induced after using the multi-step compression technique, mainly due to the overlap compression regions. Cold-Rolling, in this case, has been found more effective, controllable and repeatable than conventional multi-step cold compression for T-section panels, where controllable RS was achieved by CR and uniformly distributed in the rolling direction. Though large tensile surface RS (i.e. up to 250 MPa) were generated after CR, some (~100 MPa) of this will be reduced by CA and by final machine finishing. In the cases examined, a cold rolling level of 1.5% provided the most RS reduction. The surface residual stresses were up to 350 MPa after CR to 3%, while only ~250 MPa by CR to 1.5%. Higher cold rolling levels also created larger deflections in the rolling direction, resulting in smaller radius T-panels. The largest deflection created by 3% CR was up to 21.5 mm compared to 13.7 mm by 1.5% CR.

5.2. RS distribution by CA

During constrained ageing, creep process further relieve the RS to within ±100 MPa. The highest RS reduction by CA is up to 53% and on average is around 40%. This is slightly higher than the RS reduction (~24–36%) by pure ageing reported in literature [13,44,45]. One important advantage of CA is that this technique can also be used to correct the curvature of the component, since bending stresses are applied to the T-section component, enabling the total stress (i.e. sum of the RS and bending stresses) to relax. Though no initial bending stresses were applied to the T-section panel in this work, the experimental and modelling work of CA presented provides accurate and validated models that will form the basis required for future studies on shape correction of T-section panel using CA, where both RS and initial bending stresses are present.

5.3. Strength properties achieved

Hardness values of around ~159 HV$_{10}$ were achieved by this process, which was found to correspond to an average yield strength of 410 MPa, which meets the industrial requirements. This value is around 4% less than that of conventional manufacturing processes since the CR and creep strain-induced dislocations promote precipitate nucleation and growth, which promote the precipitation and result in a relatively non-uniform and severe over-aged precipitate patterns. The core material is stronger (i.e. ~165 HV10) than that (i.e. ~155 HV$_{10}$) of the surface material, due to the RS relaxation induced dislocations that caused over–ageing.
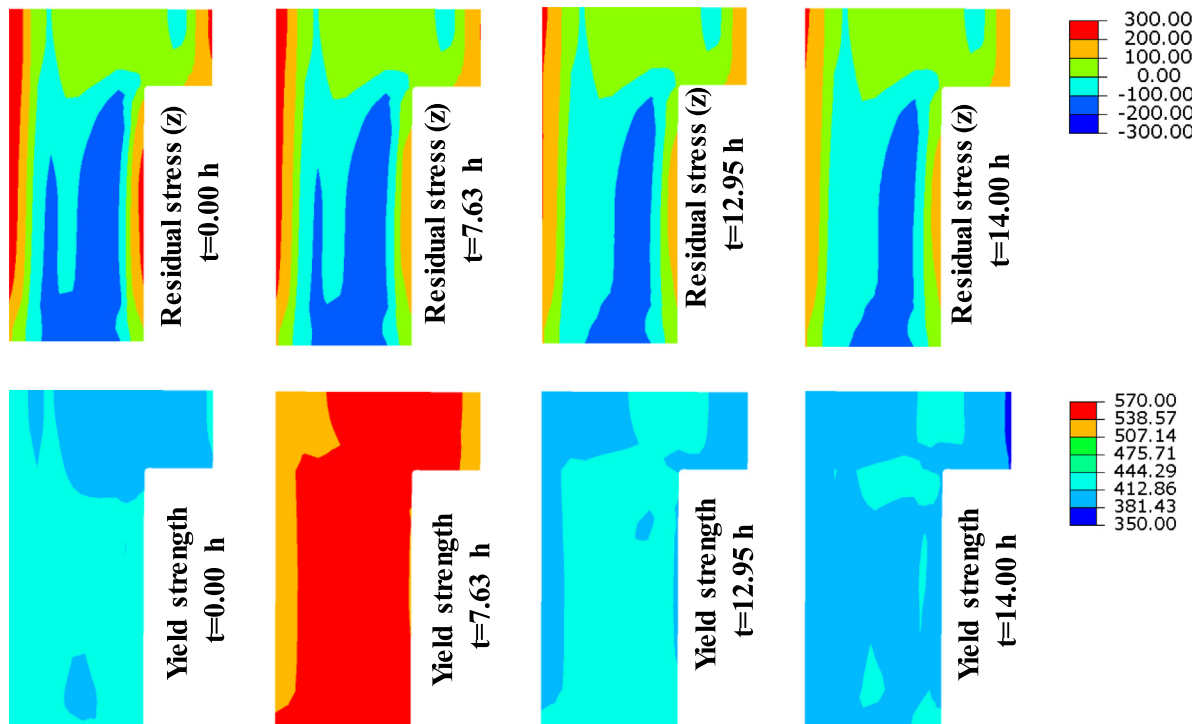

Fig. 18. The predicted evolution of residual stresses (in the rolling direction) and yield strength distributions during constrained ageing at t = 0.00, 7.63 (peak strength), 12.95, 14.00 h. Note that the unit is MPa.

5.4. Process modelling

Three FE models were developed to predict the residual stress distributions for water quenched, cold rolled and constrained aged T-section panels, respectively, employing constitutive models previously validated using uniaxial tensile, compression and stress relaxation ageing test data. Excellent agreement was achieved between the experimental and predicted RS results. Additionally, the constrained ageing model can predict the evolution of microstructure and thus yield strength distribution. The predicted average yield strength was within 2% of the experimental results and the yield strength was found to be relatively high in the core while slightly lower values near the surface of the component.

The FE simulation results indicate that after constrained ageing, smaller precipitates ($\sim 1.47 r_c$) and higher yield strength (~ 430 MPa) exist in the core part of the T-section. In contrast, the largest precipitates ($\sim 1.57 r_c$) and smallest yield strength (~ 375 MPa) were located on the surface of the web. In addition, from the predicted yield strength evolution during the constrained ageing, it can be concluded that a shorter constrained ageing time (~ 13 h) benefits the final production. This ageing time is not only sufficient for the RS reduction, where RS all reduced to within ± 100 MPa, but also considers the reduction in the material strength due to the RS relaxation during ageing, and thus leading to an overall increase in the final strength of the processed part from ~ 400 MPa to ~ 420 MPa.

6. Conclusions

A novel manufacturing process (i.e. quenching, cold rolling and T74 constrained ageing) has been developed that newly enables low residual stresses (RS) while achieving the required mechanical properties for 7050. This process has been experimentally demonstrated on scaled-down T-section components and numerically modelled. Quenching induced residual stresses (up to 300 MPa) have been successfully reduced to within ~ 100 MPa by the process. Unlike conventional techniques, the cold-rolling process developed results in uniform plastic deformation along the component, producing repeatable and predictable RS distributions, which are relatively uniform in the core of the component, thus enabling part distortion to be predicted and controlled. Additionally, the constraint ageing (CA) process developed further reduced the RS by $\sim 40\%$ and achieves an average hardness value ~ 159 HV_{10}, meeting industrial requirements.

An integrated FE model, containing three steps (WQ, CR and CA model) and incorporating two sets of constitutive equations, was established and validated by the experimental RS distributions. The CA model also successfully predicted the yield strength evolution during CA. Excellent agreements for both RS and yield strength distributions have been achieved. From CA simulation results, it is suggested that ~ 13 h CA (i.e. as opposed to 14 h in conventional T74 ageing) provides sufficient residual stress relaxation without overly sacrificing material strength of the precipitation-hardened alloy.

The novel methodology and models developed in this work, validated on a scaled-down T section geometry, provides a tool to simulate the manufacturing process of very long, complex-shaped industrial components, such as aircraft panels. The simulations which enable RS and the yield strength predictions are invaluable for process optimisation. This novel methodology provides an improved solution to mitigate the detrimental problems of part distortion in very long components, thus can provide great industrial benefits, including higher yield rates and subsequently reduced financial losses.

CRediT authorship contribution statement

Jing-Hua Zheng: Conceptualization, Data curation, Formal analysis, Software, Validation, Visualization, Writing - original draft, Writing - review & editing. **Ran Pan:** Data curation, Formal analysis, Software, Visualization. **Robert C. Wimpory:** Data curation, Formal analysis, Resources, Visualization. **Jianguo Lin:** Conceptualization, Formal analysis, Funding acquisition, Resources, Supervision, Writing - review & editing. **Chen Li:** Funding acquisition, Resources. **Catrin M. Davies:** Conceptualization, Data curation, Formal analysis, Funding acquisition, Resources, Supervision, Writing - review & editing.

References

[1] A. Heinz, A. Haszler, C. Keidel, S. Moldenhauer, R. Benedictus, W.S. Miller, Recent development in aluminium alloys for aerospace applications, Mater. Sci. Eng. A 280 (2000) 102–107.

[2] I.J. Polmear, 3 - Wrought aluminium alloys, in: I.J. Polmear (Ed.), Light Alloys, fourth editionButterworth-Heinemann, Oxford 2005, pp. 97–204.

[3] D.A. Tanner, J.S. Robinson, Residual stress prediction and determination in 7010 aluminum alloy forgings, Exp. Mech. 40 (1) (2000) 75–82.

[4] J.S. Robinson, T. Pirling, C.E. Truman, T. Panzner, Residual stress relief in the aluminium alloy 7075, Mater. Sci. Technol. 33 (2017) 1765–1775.

[5] J.K. Rai, A. Mishra, U.R.K. Rao, Residual stresses due to quenching process, International Journal of Machine Tool Design and Research 20 (1980) 1–8.

[6] M. Koç, J. Culp, T. Altan, Prediction of residual stresses in quenched aluminum blocks and their reduction through cold working processes, J. Mater. Process. Technol. 174 (2006) 342–354.

[7] N. Chobaut, D. Carron, S. Arsène, P. Schloth, J.M. Drezet, Quench induced residual stress prediction in heat treatable 7xxx aluminium alloy thick plates using Gleeble interrupted quench tests, J. Mater. Process. Technol. 222 (2015) 373–380.

[8] R.R. Nair, R. Natarajan, U.R.K. Rao, Analysis of residual stresses due to quenching considering microstructural transformations, International Journal of Machine Tool Design and Research 22 (1982) 309–319.

[9] W.-M. Sim, Challenges of residual stress and part distortion in the civil airframe industry, Int. J. Microstruct. Mater. Prop. 5 (2010).

[10] Y. Altschuler, T. Kaatz, B. Cina, Mechanical relaxation of residual stresses, ASTM, STP 993 (1988) 19–29.

[11] J.S. Robinson, S. Hossain, C.E. Truman, A.M. Paradowska, D.J. Hughes, R.C. Wimpory, M.E. Fox, Residual stress in 7449 aluminium alloy forgings, Mater. Sci. Eng. A 527 (2010) 2603–2612.

[12] G.M. Orner, S.A. Kulin, Development of stress relief treatments for high strength aluminium alloys, Manlab Inc., Cambridge, 1965.

[13] J.S. Robinson, D.A. Tanner, Residual stress development and relief in high strength aluminium alloys using standard and retrogression thermal treatments, Mater. Sci. Technol. 19 (2003) 512–518.

[14] W. Zhang, X. Wang, Y. Hu, S. Wang, Predictive modelling of microstructure changes, micro-hardness and residual stress in machining of 304 austenitic stainless steel, Int. J. Mach. Tools Manuf. 130–131 (2018) 36–48.

[15] F. Valiorgue, J. Rech, H. Hamdi, P. Gilles, J.M. Bergheau, 3D modeling of residual stresses induced in finish turning of an AISI304L stainless steel, Int. J. Mach. Tools Manuf. 53 (2012) 77–90.

[16] V. García Navas, O. Gonzalo, I. Bengoetxea, Effect of cutting parameters in the surface residual stresses generated by turning in AISI 4340 steel, Int. J. Mach. Tools Manuf. 61 (2012) 48–57.

[17] C. Shet, X. Deng, Residual stresses and strains in orthogonal metal cutting, Int. J. Mach. Tools Manuf. 43 (2003) 573–587.

[18] U.S. Dixit, P.M. Dixit, A study on residual stresses in rolling, Int. J. Mach. Tools Manuf. 37 (1997) 837–853.

[19] J.S. Robinson, D.A. Tanner, S. van Petegem, A. Evans, Influence of quenching and aging on residual stress in Al–Zn–Mg–Cu alloy 7449, Mater. Sci. Technol. 28 (2012) 420–430.

[20] D.A. Lados, D. Apelian, L. Wang, Minimization of residual stress in heat-treated Al–Si–Mg cast alloys using uphill quenching: mechanisms and effects on static and dynamic properties, Mater. Sci. Eng. A 527 (2010) 3159–3165.

[21] E.C.A. Simencio, L.C.F. Canale, G.E. Totten, Uphill quenching of aluminium: a process overview, International Heat Treatment and Surface Engineering 5 (2011) 26–30.

[22] D.A. Tanner, J.S. Robinson, Residual stress magnitudes and related properties in quenched aluminium alloys, Mater. Sci. Technol. 22 (2006) 77–85.

[23] J.S. Robinson, P.J. Tiernan, J.F. Kelleher, Effect of post-quench delay on stress relieving by cold compression for the aluminium alloy 7050, Mater. Sci. Technol. 31 (2015) 409–417.

[24] Q. Zhang, W. Zhang, Y. Liu, Evaluation and mathematical modeling of asymmetric tensile and compressive creep in aluminum alloy ZL109, Mater. Sci. Eng. A 628 (2015) 340–349.

[25] R. Pan, Z. Shi, C.M. Davies, C. Li, M. Kaye, J. Lin, An integrated model to predict residual stress reduction by multiple cold forging operations in extra-large AA7050 T-section panels, Proceedings of the Institution of Mechanical Engineers, Part B: Journal of Engineering Manufacture 232 (8) (2016) 1319–1330.

[26] I.J. Polmear, 2 - Physical metallurgy of aluminium alloys, in: I.J. Polmear (Ed.), Light Alloys, fourth editionButterworth-Heinemann, Oxford 2005, pp. 29–96.

[27] J. Lin, K.C. Ho, T.A. Dean, An integrated process for modelling of precipitation hardening and springback in creep age-forming, Int. J. Mach. Tools Manuf. 46 (2006) 1266–1270.

[28] Y. Li, Z. Shi, J. Lin, Y.-L. Yang, P. Saillard, R. Said, Effect of machining-induced residual stress on springback of creep age formed AA2050 plates with asymmetric creep-ageing behaviour, Int. J. Mach. Tools Manuf. 132 (2018) 113–122.

[29] K.C. Ho, J. Lin, T.A. Dean, Modelling of springback in creep forming thick aluminum sheets, Int. J. Plast. 20 (2004) 733–751.

[30] J. Ahn, E. He, L. Chen, R.C. Wimpory, J.P. Dear, C.M. Davies, Prediction and measurement of residual stresses and distortions in fibre laser welded Ti-6Al-4V considering phase transformation, Mater. Des. 115 (2017) 441–457.

[31] G.S. Schajer, Practical Residual Stress Measurement Methods, A John Wiley & Sons, Ltd., 2013

[32] µ-X360 Portable X-ray Residual Stress Analyzer, https://products4engineers.nl/images/default/ApaJU1-pdf.pdf (in).

[33] R. Pan, T. Pirling, J. Zheng, J. Lin, C.M. Davies, Quantification of thermal residual stresses relaxation in AA7xxx aluminium alloy through cold rolling, J. Mater. Process. Technol. 264 (2019) 454–468.

[34] J.S. Robinson, D.A. Tanner, C.E. Truman, R.C. Wimpory, Measurement and prediction of machining induced redistribution of residual stress in the aluminium alloy 7449, Exp. Mech. 51 (2011) 981–993.

[35] J.-H. Zheng, R. Pan, C. Li, W. Zhang, J. Lin, C.M. Davies, Experimental investigation of multi-step stress-relaxation-ageing of 7050 aluminium alloy for different pre-strained conditions, Mater. Sci. Eng. A 710 (2018) 111–120.

[36] W.P. Davey, Precision measurements of the lattice constants of twelve common metals, Phys. Rev. 25 (1925) 753–761.

[37] D.A. Tanner, J.S. Robinson, Effect of precipitation during quenching on the mechanical properties of the aluminium alloy 7010 in the W-temper, J. Mater. Process. Technol. 153-154 (2004) 998–1004.

[38] J.-H. Zheng, J. Lin, J. Lee, R. Pan, C. Li, C.M. Davies, A novel constitutive model for multi-step stress relaxation ageing of a pre-strained 7xxx series alloy, Int. J. Plast. 106 (2018) 31–47.

[39] R. Pan, A novel process for forming T-section components with low residual stresses in aluminium alloys, Mechanical Engineering, Imperial College London, 2017.

[40] T.A. Stolariski, S. Tobe, Rolling Contacts, John Wiley and Sons Ltd, Bury St Edmunds, United Kingdom, 2001.

[41] M. Tiryakioğlu, J.S. Robinson, M.A. Salazar-Guapuriche, Y.Y. Zhao, P.D. Eason, Hardness–strength relationships in the aluminum alloy 7010, Mater. Sci. Eng. A 631 (2015) 196–200.

[42] J.C. Werenskiold, A.Y. Bréchet, Characterization and modeling of precipitation kinetics in an Al–Zn–Mg alloy, Mater. Sci. Eng. A 293 (2000) 267–274.

[43] D.A. Tanner, J.S. Robinson, Modelling stress reduction techniques of cold compression and stretching in wrought aluminium alloy products, Finite Elem. Anal. Des. 39 (2003) 369–386.

[44] M.S. Younger, K.H. Ecklmeyer, Overcoming Residual Stresses and Machining Distortion in the Production of Aluminum Alloy Satellite Boxes in, United States, 2007.

[45] J.S. Robinson, D.A. Tanner, S.D. Whelan, Retrogression, reaging and residual stresses in 7010 forgings, Fatigue Fract. Eng. Mater. Struct. 22 (1999) 51–58.

[46] W.M. Baldwin, Residual stresses in metals, 1949 Philadelphia.